

Distortion-driven Turbulence Effect Removal using Variational Model

Yuan Xie, *Member, IEEE*, Wensheng Zhang, Dacheng Tao, *Senior Member, IEEE*, Wenrui Hu,
Yanyun Qu, and Hanzi Wang, *Senior Member, IEEE*,

Abstract

It remains a challenge to simultaneously remove geometric distortion and space-time-varying blur in frames captured through a turbulent atmospheric medium. To solve, or at least reduce these effects, we propose a new scheme to recover a latent image from observed frames by integrating a new variational model and distortion-driven spatial-temporal kernel regression. The proposed scheme first constructs a high-quality reference image from the observed frames using low-rank decomposition. Then, to generate an improved registered sequence, the reference image is iteratively optimized using a variational model containing a new spatial-temporal regularization. The proposed fast algorithm efficiently solves this model without the use of partial differential equations (PDEs). Next, to reduce blur variation, distortion-driven spatial-temporal kernel regression is carried out to fuse the registered sequence into one image by introducing the concept of the near-stationary patch. Applying a blind deconvolution algorithm to the fused image produces the final output. Extensive experimental testing shows, both qualitatively and quantitatively, that the proposed method can effectively alleviate distortion and blur and recover details of the original scene compared to state-of-the-art methods.

Index Terms

Image restoration, atmospheric turbulence, variational model, distortion-driven kernel

I. INTRODUCTION

Atmospheric turbulence can severely degrade the quality of images produced by long range observation systems, rendering the images unsuitable for vision applications such as surveillance or scene inspection. The main visual effects caused by atmospheric turbulence are geometric distortion and space-time-varying blur (see examples in Fig. 1). The distortion is primarily generated by (1) optical turbulence and (2) scattering and absorption by particulates;

Y. Xie, W. Zhang and W. Hu are with the State Key Lab. of Complex Systems and Intelligence Science, Institute of Automation, Chinese Academy of Sciences, Beijing, 100190, China; E-mail: {yuan.xie, wensheng.zhang, wenrui.hu}@ia.ac.cn

D. Tao is with the Center for Quantum Computation & Intelligent Systems and the Faculty of Engineering & Information Technology, University of Technology, Sydney, Australia; E-mail: dacheng.tao@uts.edu.au

Y. Qu and H. Wang are with School of Information Science and Technology, Xiamen University, Fujian, 361005, China; E-mail: {yyqu, hanzi.wang}@xmu.edu.cn

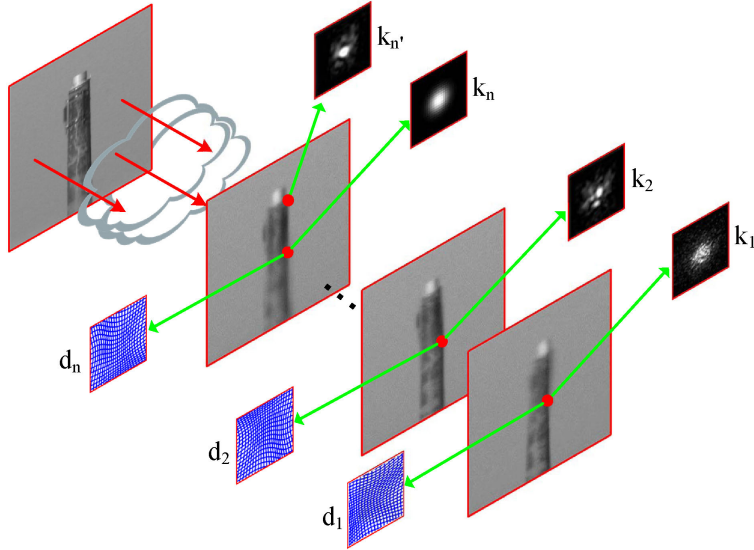


Figure 1. Illustration of the visual effects caused by atmospheric turbulence. d_1 to d_n are local deformation fields, which means that a distortion effect exists. Blur kernels k_1 to k_n and k'_n indicate the space-time-varying blur effect.

aerosols, for example, diffuse light will also cause blur [1]. Several approaches have been used to restore images, including adaptive optics techniques (*e.g.* [2], [3]) and pure image processing-based methods (such as [4], [5], [6], [7], [8]). Due to random fluctuations in turbulence, calculating a reasonable estimation of atmospheric modulation transfer function (MTF) is extremely difficult. However, this function is of critical importance for optics-based restoration methods. Therefore, in this article, we only focus on using image processing to handle the degradation caused by turbulence. Supposing that the scene and the image sensor are both static, we adopt the mathematical model used in [7], [9], [10] to interpret imaging processing through the turbulence:

$$f_i(\mathbf{x}) = D_{i,blur(\mathbf{x})}(H(u(\mathbf{x}))) + \varepsilon_i, \quad \forall i, \quad i \in [1, \dots, N] \quad (1)$$

where u is the static original scene needed to be retrieved, f_i is the observed frame at time i , N represents the number of observed frames, the vector $\mathbf{x} = (x, y)^T$ is a 2-D spatial location, and ε_i denotes the sensor noise. H is a blurring operator, which is caused by sensor optics, and corresponds to a space-invariant diffraction-limited point spread function (PSF) h . D is a deformation operator, and its subscript indicates that both the local deformation and the space-varying blur (the PSF is characterized by $h_{i,x}$) exist concurrently.

Simultaneously removing space-time-varying blur and distortion is a nontrivial problem. Li *et al.* [11] explicitly formulated multichannel image deconvolution as a principal component analysis (PCA) problem, and applied it to the restoration of atmospheric turbulence-degraded images. However, this spectral method does not fully correct the deformation. Moreover, due to the fact that high-frequency information is discarded, the local texture of the true scene is also poorly recovered. Hirsch *et al.* [9] utilized space-varying blind deconvolution to alleviate turbulence distortion. While reasonably effective, it does not take sensor noise into account when estimating the local PSF, which results in deblurring artifacts.

Image selection and fusion methodologies have been deployed to produce a high-quality latent image. The “lucky frame” methods [12], [13], [14], [15] select the relatively high quality frame from a degraded sequence by using sharpness as the image quality measurement. However, the so-called “lucky frame” is unlikely to exist in a short exposure video stream. To alleviate this problem, Aubailly *et al.* [16] proposed a local version of the “lucky frame” method referred to as the “lucky region” method. In this method, a high-quality image from the output is fused with many small lucky regions detected using a local sharpness metric. However, even though the space-time-varying blur can be removed during the fusion process, the final output is still susceptible to the blur caused by the diffraction-limited PSF [7].

The success of some recently proposed turbulence removal methods stems from the use of diffeomorphic warping and image sharpening techniques [8], [17], [18], [19]. Shimizu *et al.* [8] applied a temporal median filter to build a reference image, and then fixed the geometric distortion using B-spline non-rigid registration associated with an additional stabilization term. A high-resolution latent image is then obtained by employing a super-resolution method. Mao and Gilles [19] combined optical flow-based geometric correction with a non-local total variance-based regularization process to recover the original scene. However, this method only focuses on correcting distortion and ignores the rich information in multiple frames when recovering the detail of the image.

Zhu *et al.* [7] proposed the diffeomorphic warping and image sharpening approach by combining a symmetric constraint-based B-spline registration associated with near-diffraction-limited image reconstruction to reduce the space and time-varying problem to a shift invariant one. However, this method has two main limitations: (1) the method uses the temporal mean of the observed frame to calculate the reference image, which leads to a poor registration result (especially in the case of strong turbulence); and (2) the method constructs a single image from the near-diffraction-limited detection based on the assumption that the distortion can be effectively removed, meaning that the noise introduced by registration error cannot be reduced.

In this paper, we propose a new scheme for restoring a single sharp image of the original scene from a sequence of observed frames degraded by atmospheric turbulence. The proposed method can effectively remove both local deformation and spatially-varying blur and recover the image details, even in the case of strong turbulence. The scheme consists of the following four steps. First, we construct a reference image by *low-rank decomposition*, resulting in a sharper and less noisy image than the traditional method. Second, the reference image is iteratively optimized and enhanced using a variational model involving a new *spatial-temporal regularization*, which helps generate an improved registered sequence. Moreover, we design *a simple but highly efficient algorithm* without the use of PDEs in order to solve the variational model, which is supported by a rigorous proof of convergence. Third, by introducing the concept of the near-stationary patch, a single image with reduced space-varying blur is produced using a fusion process. In this step, to avoid noise effects, *distortion-driven spatial-temporal kernel regression* is employed to eliminate the noise both in the image and the temporal domains. To the best of our knowledge, using the information from the deformation field to guide the construction of the local kernel has not previously been described. Finally, a blind space-invariant deconvolution algorithm can be used to generate the final output.

This paper is structured as follows. Section II provides an overview of the proposed restoration algorithm. In

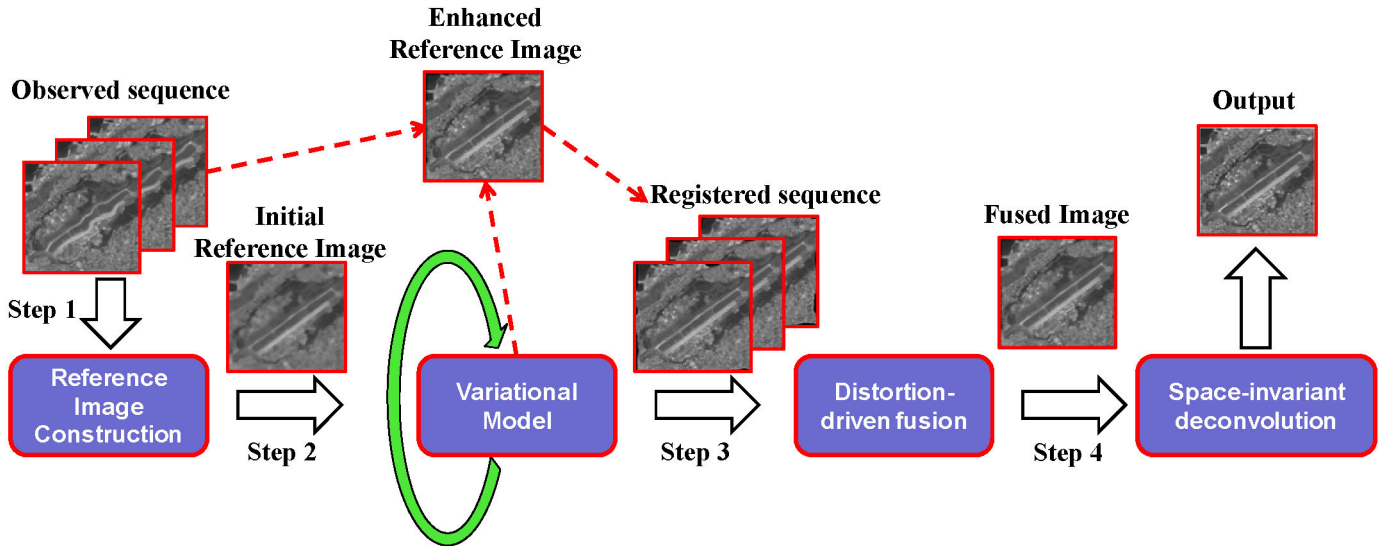


Figure 2. Block diagram of the proposed restoration scheme. (1) Step 1: construct a high-quality reference image from observed sequence using low-rank decomposition; this reference image will be used as the initial value of the variational model in the next step. (2) Step 2: enhance the reference image iteratively using a new variational model (as the green arrow shown). After the convergence of optimization, the observed sequence is registered to the enhanced reference image to produce a registered sequence with little local deformation (as the dashed arrow line indicated). (3) Step 3: a distortion-driven fusion process is employed to fuse the registered sequence to one image with only space-invariant blur effect existing. (4) Step 4: final restored image is produced by a commonly space-invariant deconvolution method.

Section III, we detail the method used to optimize the reference image. Image fusion from the registered sequence is presented in Section IV, while single image deconvolution is presented in Section V. Experimental results are presented in Section VI and we discuss the methods and conclude in Section VII.

II. RESTORATION SCHEME OVERVIEW

The proposed restoration framework has four main steps (see Fig. 2). Given an observed sequence $\{f_i\}$, step 1 applies the low-rank decomposition to $\{f_i\}$ to generate a high-quality reference image. In multi-frame registration, the reference image is usually obtained by computing the temporal mean of the observed frames [6], [7], [8], [17], [18], [19], [20]. An averaged image such as this is always blurry and noisy, especially when turbulence is strong. Inspired by [21], which utilizes sparse decomposition for background modeling, we use matrix decomposition to obtain the low-rank part and construct the reference image for registration. Our rationale for using this approach is that the low-rank part is a stable component of a "dancing image", and therefore corresponds to the original scene to some extent. The decomposition can be defined as follows:

$$\text{minimize } \|L\|_* + \lambda\|S\|_1 \quad \text{subject to } L + S = G \quad (2)$$

where $G \in R^{m \times n}$ is the distorted sequence matrix with each column being a distorted frame vector f_i , m denotes the total pixels in each frame, and n denotes the number of frames in the sequence. $L \in R^{m \times n}$ is the low-rank component of G , $S \in R^{m \times n}$ is the sparse component of G , $\|\cdot\|_*$ is the nuclear norm defined by the sum of all

singular values, $\|\cdot\|_1$ is the l_1 -norm defined by the component-wise sum of absolute values of all the entries, and λ is a constant providing a trade-off between the sparse and low-rank components. Some decomposed results are illustrated in Fig. 3. We exploit robust principal component analysis (RPCA) to estimate the reference image, which acts as the initial value for the next step.

Step 2 enhances the reference image using a variational model employing spatial-temporal regularization. This optimization is the inverse process of the following problem

$$f_i = \Phi_i u + \varepsilon, \quad \forall i \in [1, \dots, N] \quad (3)$$

where Φ_i is the linear operator corresponding to the deformation field \overleftarrow{F}_i obtained by B-spline registration [22], [23] and u represents the reference image to be enhanced. The variational model optimizes with only a few rounds of non-rigid registration and subproblem optimization. After the convergence of the optimization procedure, the observed frames $\{f_i\}$ are registered to the enhanced reference image to achieve the registered sequence $\{R_i\}$. This step effectively removes local deformation.

Step 3 restores a single image Z from the registered sequence $\{R_i\}$ by distortion-driven fusion in order to eliminate the space-time-varying blur. A near-stationary patch can be detected for each local region from the patch sequence through the temporal domain. Spatial-temporal kernel regression is then carried out to reduce the noise caused by optics and registration error. Fusing all the denoised near-stationary patches generates an image Z . While the output Z is still a blurred image, it can be approximately restored using a common spatially invariant deblurring technique.

In the final step, based on the statistical prior of natural images, a single image blind deconvolution algorithm is implemented on Z to further remove blur and enhance image quality. Details of steps 3, 4 and 5 will be given in the following sections.

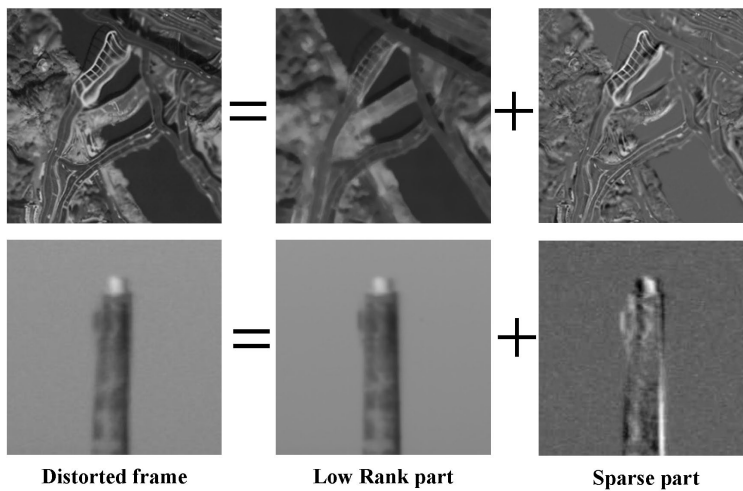


Figure 3. Low-rank decomposition of the distorted frames in city_strong and chimney sequences

III. OPTIMIZE THE REFERENCE IMAGE USING A VARIATIONAL MODEL

The obtained reference image from RPCA is not completely ready for non-rigid registration because the inner structure of the reference image cannot be easily recovered. In other words, the edges representing the object's profile tend to be well defined, while the edges that characterize the inner structure of the object tend to be intermittent and noisy. Therefore, the reference image needs to be refined. Assuming that the observed image sequence is $\{f_i\}_{i=1}^N$ and the reference image that we want to optimize is u , then directly reconstructing u from Eq. (3) is an ill-posed problem. There is a need to introduce a regularization technique. If we denote the regularization term of the image as $J(u)$, then we can get an unconstrained optimization problem

$$\min_u E(u) + J(u) \quad (4)$$

$$= \min_u \underbrace{\sum_i \|\Phi_i u - f_i\|_2^2}_{E(u)} + \underbrace{(\mu_1 J_s(u) + \mu_2 J_t(u))}_{J(u)} \quad (5)$$

$$= \min_u \underbrace{\sum_i \|\Phi_i u - f_i\|_2^2}_{E(u)} + \underbrace{(\mu_1 \overbrace{|u|_{NLTV}}^{J_s(u)} + \mu_2 \overbrace{|(u - u_p)|_{TV}}^{J_t(u)})}_{J(u)} \quad (6)$$

where $E(u)$ measures the fidelity of the observed data, and $J(u)$ includes the spatial regularizer $J_s(u)$ and the temporal regularizer $J_t(u)$ to constraint the solution of u . $J_s(u)$ is the non-local total variation which can explore repetitive structures to preserve important details of an image while effectively removing artifact. $J_t(u)$ is the standard total variation of the difference between two consecutively optimized results (u_p denotes the result obtained by the previous step), which does not only restrict the smoothness between the iterations but also forces the local energy of the optimized result to converge to a local structure (*e.g.* the edge of the object). The parameters μ_1 and μ_2 are chosen as a trade-off between the two regularizers. Because $J(u)$ applies the sparsifying transform in both the spatial and temporal domains, we refer to it as the **spatial-temporal regularization**. In the following subsections, we develop a fast algorithm to solve the optimization problem (6).

A. Optimization by Bregman Iteration

Bregman iteration is a concept that originated from functional analysis and is commonly used to find the extrema of convex functions [24]. It was introduced in [25] for total variation-based image processing, before being extended to other applications such as wavelet-based denoising [26] and magnetic resonance imaging [27]. In this subsection, we briefly describe how to restore the optimization problem (6) using this technique.

The Bregman distance [24] associated with a convex function J between points u and v is

$$D_J^p(u, v) = J(u) - J(v) - \langle p, u - v \rangle \geq 0, \text{ where } p \in \partial J(v) \quad (7)$$

where p is the subgradient of J at v . Because $D_J^p(u, v) \neq D_J^p(v, u)$, $D_J^p(u, v)$ is not a distance in the usual sense. However, it measures the closeness between u and v in the sense that $D_J^p(u, v) > 0$, and $D_J^p(u, v) \geq D_J^p(w, v)$

for any point w being a convex combination of u and v . According to [25], and using the Bregman distance, the optimization problem (6) can be solved by the following iteration

$$\begin{cases} u^k = \operatorname{argmin}_u \mu J(u) + \sum_{i=1}^N \|\Phi_i u - f_i^k\|^2 & (8a) \\ f_i^{k+1} = f_i^k + f_i - \Phi_i u^k & (8b) \end{cases}$$

where $f_i^0 = f_i$. It has been proved in [25] that the above iteration converges to the solution of (6). Moreover, as shown in [28], [29], Bregman iteration is actually equivalent to alternatively decreasing the primal variable and increasing the dual variable of the Lagrangian of the problem (6).

In subproblem (8a), the data-fidelity term $E(u)$ co-occurs with the regularization term $J(u)$, which leads to a sophisticated solution. However, this subproblem can be solved efficiently using the forward-backward operator splitting method [30], [31], [32]:

$$\begin{cases} v^{k+1} = u^k - \delta \sum_{i=1}^N \Phi_i^T (\Phi_i u^k - f_i^k) & (9a) \\ u^{k+1} = \operatorname{argmin}_u \left(\mu J(u) + \frac{1}{2\delta} \|u - v^{k+1}\|^2 \right) & (9b) \end{cases}$$

where Φ_i^T denotes the adjoint operator of Φ_i . The parameter δ is set to 1 in experiments. The advantage of the above method is the separation of Φ_i and $J(u)$. The first step is called the forward step, which is actually the gradient descent of the data-fidelity term $E(u)$, and the second step is called the backward step, which can be solved efficiently for many choices of regularizer $J(u)$. For example, if we choose the total variation as the regularizer, then the subproblem is actually a standard Rudin-Osher-Fatemi (ROF) model [33], which can be efficiently solved via the graph-cut [34] or the split Bregman method [35]. In our method, $J(u)$ is a mixed regularizer that contains non-local total variation (TV) and TV, so we refer to the subproblem (9b) as the mixed-ROF model.

B. Finding an Efficient Solution for the Mixed-ROF Model

No matter which ROF-like model we choose, current approaches always involve solving PDEs in each iteration, including the split Bregman method [28], [35]. Here, we extend the method proposed in [36], which only handles the standard ROF model, to the general mixed ROF case, and provide a very simple but highly efficient and effective optimization algorithm without using PDEs. By replacing $J(u)$ with $J_s(u)$ and $J_t(u)$, the subproblem (9b) can be expanded as follows:

$$\min_u \mu_1 |\nabla_w u|_1 + \mu_2 \left(|\nabla_x(u - u_p)|_1 + |\nabla_y(u - u_p)|_1 \right) + \frac{1}{2} \|u - v\|_2^2 \quad (10)$$

The following new iteration schema can find the unique solution u^* efficiently for the minimization problem (10).

Let $b_w^0 = 0, b_x^0 = 0, b_y^0 = 0$ and $u^1 = v$, for $k = 1, 2, \dots$, the iteration is as follows:

$$b_w^k = \text{cut}(\nabla_w u^k + b_w^{k-1}, \frac{\mu_1}{\lambda_1}) \quad (11)$$

$$b_x^k = \text{cut}(\nabla_x u^k - \nabla_x u_p + b_x^{k-1}, \frac{\mu_2}{\lambda_2}) \quad (12)$$

$$b_y^k = \text{cut}(\nabla_y u^k - \nabla_y u_p + b_y^{k-1}, \frac{\mu_2}{\lambda_2}) \quad (13)$$

$$u^{k+1} = v + \frac{\lambda_1}{\mu_1} \text{div}_w b_w^k - \frac{\lambda_2}{\mu_2} (\nabla_x^T b_x^k + \nabla_y^T b_y^k) \quad (14)$$

where $\text{shrink}(x, \gamma) = x - \frac{x}{|x|} * \max(|x| - \gamma, 0)$.

In the above equations, ∇_x and ∇_y are the difference operators along the x and y directions, respectively, ∇_w denotes the non-local gradient operator, and div_w is the non-local graph divergence operator (see the detailed mathematical definitions of all these operators in the Appendix). We prove the convergence of the proposed fast algorithm in the following theorem:

Theorem 1. For $k = 1, 2, \dots$, let b_w^k, b_x^k, b_y^k and u^{k+1} be given by the iteration (11) to (14). If $0 < 20\lambda_1 + 4\lambda_2 < 1$, then $\lim_{k \rightarrow \infty} u^k = u^*$.

Proof: See the proof in Section VIII-B. ■

IV. DISTORTION-DRIVEN IMAGE FUSION

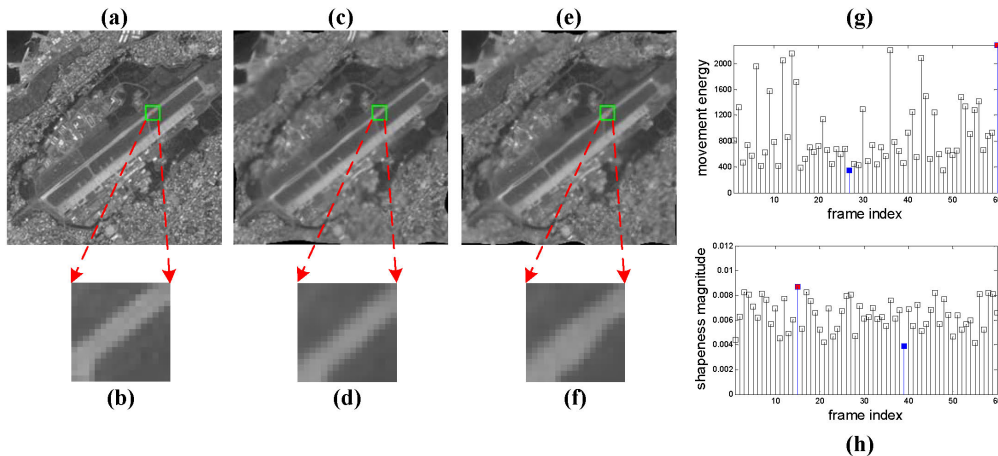


Figure 4. Near-stationary patch vs. near-diffraction-limited patch in the airport sequence. (a) Ground truth; (b) Zoomed ground truth patch from (a); (c) Frame contains near-stationary patch; (d) Zoomed near-stationary patch from (c); (e) Frame contains near-diffraction-limited patch; (f) Zoomed near-diffraction-limited patch from (e); (g) Movement energy of the local patch over 60 frames; (h) Intensity variance of local patch over 60 frames.

In this section, by introducing the concept of the **near-stationary patch**, we fuse the registered sequence $\{R_k\}$ into a single image Z , which can be deblurred using a space-invariant deconvolution method. The fusion steps are summarized in Algorithm 1. Different from our approach, [7] builds the image Z by fusing the diffraction-limited

Algorithm 1: Procedure for reconstructing a stationary image from registered frames

- 1 Given a registered sequence $\{R_k\}$ and the push-forward motion field sequence $\{\overleftarrow{F}_k\}$ by inverting $\{\overrightarrow{F}_k\}$, divide each frame into $L \times L$ overlapping patches centered at each pixel, and calculate the intensity variance and the movement energy of each patch as a local stationary measure.
 - 2 For a patch sequence $\{r_k\}$ centered at location \mathbf{x} , detect the most stationary one r_{k^*} by local variance and movement energy.
 - 3 Set r_{k^*} as a reference patch, and restore its center pixel value using spatial-temporal kernel regression. Assign this value to the pixel $Z[\mathbf{x}]$.
 - 4 Go to the next pixel and return to step 2.
-

patches, which can be detected using local sharpness measures. However, due to the registration error, some detected diffraction-limited patches still contain local distortion. Examples are shown in Fig. 4 where the patches (d) and (f) are obtained by near-stationary detection and near-diffraction-limited detection, respectively. Compared with (f), the near-stationary patch (d) shows less local deformation and more closely resembles the latent true patch (b). Therefore, employing a local sharpness measure alone is insufficient to recover the image details. In the following subsections, we will first describe how to detect near-stationary patches, and then detail the proposed distortion-driven spatial-temporal kernel regression used for reducing the noise caused by sensor and registration errors during the fusion process.

A. Near-Stationary Patch Detection

In turbulence free or near turbulence free conditions, the light reflected from the scene through the atmosphere is perpendicular to the camera. Therefore, any scene inside local regions should be clearly observed by the camera without distortion or blur. Such local regions are referred to as stationary patches. Suppose the k^* -th patch is found to be near-stationary: we propose to detect this near-stationary patch by taking both local sharpness and local movement energy into account. According to [7], the local sharpness of a $L \times L$ patch is determined by its variance in intensity, which is

$$s_{\mathbf{x}}^k = \frac{1}{L^2 - 1} \sum_{\mathbf{x}} (r_k[\mathbf{x}] - \bar{r}_k)^2 \quad (15)$$

where \bar{r}_k represents the mean value of patch r_k . For further details on the $s_{\mathbf{x}}^k$ calculation, please refer to [7].

The local movement energy of an $L \times L$ patch r_k can be calculated as:

$$e_{\mathbf{x}}^k = \sum_{\mathbf{x} \in \Omega(r_k)} |\overleftarrow{f}_k[\mathbf{x}]|^2 \quad (16)$$

where $\overleftarrow{f}_k[\mathbf{x}]$ denotes the deformation vector at position \mathbf{x} from the k -th deformation field in sequence $\{\overleftarrow{F}_i\}$ (the deformation field \overrightarrow{F}_i , which warps the distorted frame f_i to the reference image, and its inverse field \overleftarrow{F}_i are calculated from B-spline registration), and $\Omega(r_k)$ is the support region of the local patch r_k . Consequently, given the stationary

measurement, we select the energy patch r_{k^*} with the lowest movement as the near-stationary patch from the ten sharpest ones in the patch sequence $\{r_k\}$. Then, r_{k^*} is used as a reference patch to restore its center pixel value; this is described in the next subsection.

B. Fusion by Spatial-Temporal Kernel Regression

This subsection describes how one single image Z is generated by fusing the detected near-stationary patches. To avoid possible artifacts that may appear during subsequent deblurring, noise in the selected near-stationary patches needs to be suppressed. Zhu and Milanfar [7] employed zero-order kernel regression to estimate the value of a pixel at \mathbf{x} in its reference frame δ by

$$\hat{q}_\delta[\mathbf{x}] = \frac{\sum_k U(\mathbf{x}; k, \delta) r_k[\mathbf{x}]}{\sum_k U(\mathbf{x}; k, \delta)} \quad (17)$$

where $U(\cdot)$ denotes a patch-wise photometric distance which can be calculated by a Gaussian kernel function

$$U(\mathbf{x}; k, \delta) = \exp\left(\frac{2\sigma_n^2}{\mu^2} - \frac{\|r_k - r_\delta\|^2}{L^2\mu^2}\right), \quad (18)$$

where σ_n^2 is the noise variance (we set $\sigma_n^2 = 2$ in our experiments), L^2 denotes the total number of pixels in the patch, and the scalar μ is the smoothing parameter [37].

However, this denoising method only takes temporal information into account and ignores the registration error in the image domain. From Fig. 4 we can see that the more the movement energy of a patch, the less likely it is to have its deformation thoroughly removed. Therefore, $r_k[\mathbf{x}]$ in Eq. (17) may not represent the true value of the pixel \mathbf{x} . Hence, to reconstruct a single image Z , a spatial-temporal kernel regression is used to restore each pixel. In the spatial domain (image domain), distortion-driven asymmetric steering kernel regression is used to remove the deviation of each central pixel of the patch of r_k . In the temporal domain, patch-wise temporal regression is used to correct the central pixel and further reduce the noise level [7]. The details of the spatial-temporal kernel regression are described in the following two subsections.

1) *Point-Wise Spatial Asymmetric Steering Kernel Regression*: Directly finding a true pixel value is a nontrivial problem. We resort to calculating $\tilde{r}_k[\mathbf{x}]$, which denotes the corrected value of a pixel at position \mathbf{x} in the registered frame R_k to replace $r_k[\mathbf{x}]$ in Eq. (17). Then, $\tilde{r}_k[\mathbf{x}]$ can be estimated using the zero-order kernel regression (Nadaraya-Watson estimator [38])

$$\tilde{r}_k[\mathbf{x}] = \frac{\sum_{x_j \in r_k} K_{dskr}(\mathbf{x}_j - \mathbf{x}) r_k[\mathbf{x}]}{\sum_{x_j \in r_k} K_{dskr}(\mathbf{x}_j - \mathbf{x})} \quad (19)$$

where $K_{dskr}(\cdot)$ represents a distortion-driven kernel function that depends on the local deformation field. Such a kernel can indicate a pixel's direction of deviation; in other words, the weights should be larger in the deviated direction (see Fig. 5 $s1$ to $s5$). Inspired by the steering kernel [39], we propose a two-step approach to construct a distortion-driven kernel function.

First, measure the dominant orientation of the local deformation field and build the symmetric kernel function. The orientation is the singular vector corresponding to the largest (nonzero) singular value of the local deformation

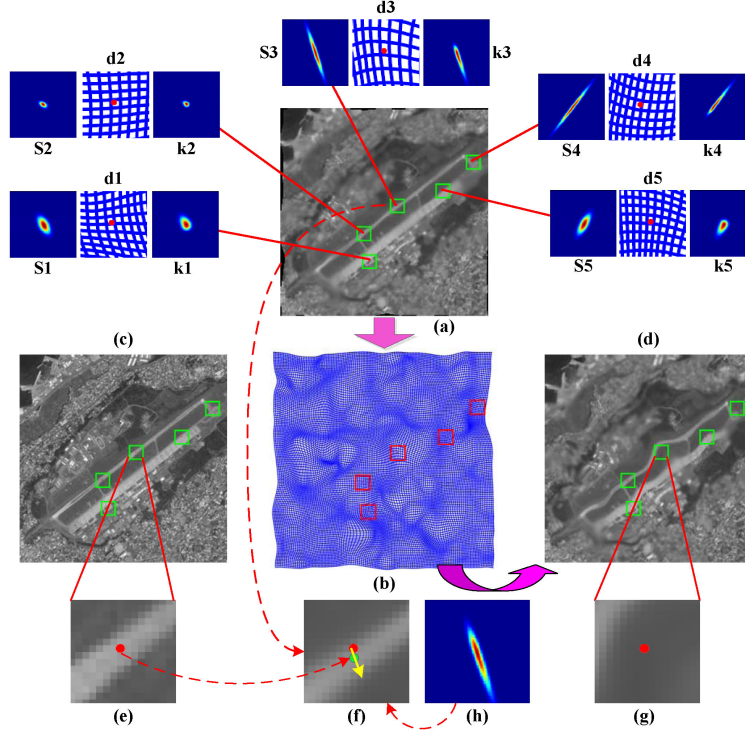


Figure 5. Illustration of distortion-driven asymmetric steering kernel.

matrix

$$M_k = \begin{bmatrix} \vdots & \vdots \\ \overleftarrow{f}_x(\mathbf{x}_j) & \overleftarrow{f}_y(\mathbf{x}_j) \\ \vdots & \vdots \end{bmatrix} = U_k S_k V_k^T, \quad \mathbf{x}_j \in \Omega(r_k), \quad (20)$$

where \overleftarrow{f}_x and \overleftarrow{f}_y are the displacement vectors along the x and y direction, and $\Omega(r_k)$ is the local support region of r_k . $U_k S_k V_k^T$ is the truncated singular value decomposition of M_k , and S_k is a diagonal 2×2 matrix representing the energy in the dominant direction. Then, in the first column of the orthogonal matrix V_k , $v_1 = [\nu_1, \nu_2]^T$ defines the dominant orientation angle $\theta_k = \arctan(\frac{\nu_2}{\nu_1})$. This means that the singular vector corresponding to the largest singular value of M_k represents the dominant orientation of the local deformation field. The elongation parameter σ_i and scaling parameter γ_i are calculated by

$$\sigma_i = \frac{s_1 + \lambda'}{s_2 + \lambda'}, \quad \lambda' \geq 0, \quad \gamma_i = \left(\frac{s_1 s_2 + \lambda''}{M} \right)^{\frac{1}{2}}, \quad (21)$$

where s_1 and s_2 are the diagonal elements of the matrix S_k , and λ' and λ'' denote the regularization parameters. Given the parameters mentioned above, we can calculate the steering kernel function as in [39] (hereafter, the symmetric steering kernel is referred to as $K_{dskr}^s(\cdot)$). Fig. 5 is a visual illustration of the steering kernel footprints for different local deformation regions. Image (a) is one registered frame from $\{R_i\}$, and the patches $d1$ to $d5$ (cropped from deformation field (b)) are the local deformation fields of the pixels marked by red dots in image (a). As shown in Fig. 5, the size and shape of each symmetric steering kernel ($s1$ to $s5$) are locally adapted to the

corresponding deformation field. For example, $s2$ is blunt due to the small movement energy of its corresponding deformation field, while $s3$ is sharp because the movement energy of $d3$ is much larger than that of $d2$.

Second, construct the asymmetric steering kernel using the dominant orientation. State-of-the-art non-rigid registration approaches are usually unable to correct a local deformation when the movement energy is very large. Nevertheless, due to the smoothness of the B-spline-based registration, the true pixel value $\tilde{r}_k[\mathbf{x}]$ often appears in the opposite direction of the dominant orientation. As shown in Fig. 5, patches (g) and (f) are cropped from one observed frame (d) and its corresponding registered frame (a), respectively, and patch (e) is cropped from the ground truth image (c) (the central pixels of (e), (f), and (g) are marked by red dots). Comparing patch (e) with patch (f), the two central pixels represent different positions due to the registration error. In fact, the central pixel of patch (e) corresponds to the pixel marked in green in patch (f). Consequently, to estimate $\tilde{r}_k[\mathbf{x}]$ more precisely, we need to further shrink the footprint of the local kernel; the weights along the inverse dominant orientation should be larger than those along the dominant orientation. Hence, we construct a local asymmetric kernel function $K_{dskr}^a(\cdot)$ by utilizing the *Asymmetric Gaussian* proposed in [40], where the dimension needed to be asymmetric can be calculated by

$$A(z_i; \mu_i^z, \rho_i^2, r_i) = \frac{2}{\sqrt{2\pi}} \frac{1}{\sqrt{\rho_i^2(r_i + 1)}} \begin{cases} \exp\left(-\frac{(z_i - \mu_i^z)^2}{2\rho_i^2}\right) & \text{if } z_i > \mu_i^z \\ \exp\left(-\frac{(z_i - \mu_i^z)^2}{2r_i^2\rho_i^2}\right) & \text{otherwise} \end{cases} \quad (22)$$

where z_i is along the dominant orientation of the symmetric kernel $K_{dskr}^s(\cdot)$, μ_i^z and ρ_i^2 are the mean and variance corresponding to z_i , and r_i denotes the asymmetric coefficient with $r_i = 1$ being equivalent to the ordinary Gaussian. In our implementation, r_i is usually set to $0.5\sqrt{\sigma_i}$, where σ_i is the elongation coefficient defined in Eq. (21). An example of an asymmetric kernel is shown in Fig. 5 $k1$ to $k5$. Due to the computational complexity, we only use spatial kernel regression for the pixels whose movement energy is greater than a pre-defined threshold. For the remaining pixels with relatively low movement energy, we directly assign $r_k[\mathbf{x}]$ to $\tilde{r}_k[\mathbf{x}]$.

2) *Patch-Wise Temporal Kernel Regression*: Once the corrected pixel value $\tilde{r}_k[\mathbf{x}]$ in each frame has been calculated, we can further estimate the pixel value at position \mathbf{x} by means of spatial-temporal kernel regression for a single image Z

$$\hat{q}_\delta[\mathbf{x}] = \frac{\sum_k U(\mathbf{x}; k, \delta) \tilde{r}_k[\mathbf{x}]}{\sum_k U(\mathbf{x}; k, \delta)} = \frac{\sum_k U(\mathbf{x}; k, \delta) \frac{\sum_{x_j \in r_k} K_{dskr}^a(\mathbf{x}_j - \mathbf{x}) r_k[\mathbf{x}]}{\sum_{x_j \in r_k} K_{dskr}^a(\mathbf{x}_j - \mathbf{x})}}{\sum_k U(\mathbf{x}; k, \delta)}. \quad (23)$$

Spatial-temporal kernel regression is illustrated in Fig. 6: the yellow box denotes the spatial regression that exploits the local deformation structure to restore a certain pixel only in the image domain, and the red line represents the temporal regression, which fuses the information across all the corrected pixels $\{\tilde{r}_k[\mathbf{x}]\}_{k=1}^N$ in the temporal domain. Due to utilization of both spatial and temporal information, we refer to such regression as the **Spatial-Temporal Kernel Regression**.

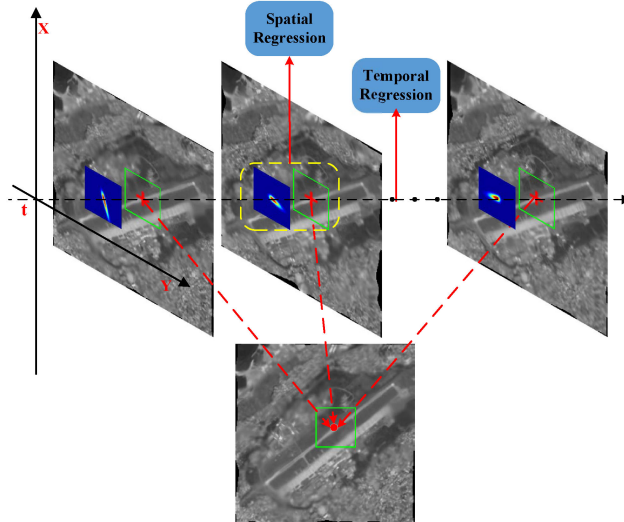


Figure 6. Illustration of distortion-driven spatial-temporal kernel regression.

V. SPACE-INVARIANT DECONVOLUTION

A post-process is needed to correct the diffraction-limited blur that still exists in Z . We exploit the blind deconvolution algorithm [41] to calculate a final output (corresponding to step 18 in Algorithm 2). In the degradation model

$$Z = L \otimes h + \varepsilon \quad (24)$$

the deblurring procedure can be described using the following optimization problem

$$\operatorname{argmin}_{F,h} \|Z - L \otimes h\|_2^2 + \gamma_1 R_f(L) + \gamma_2 R_h(h) \quad (25)$$

where ε denotes the error caused by the fusion process in Section IV, and R_f and R_h are the regularizers used to restrict the latent sharp image L and the blur kernel h based on their own prior knowledge. As suggested in [41], the regularization term for L is defined as

$$R_f(L) = \|\rho(\partial_x L) + \rho(\partial_y L)\|_1 \quad (26)$$

where $\partial_x L$ and $\partial_y L$ represent the derivatives of L in horizontal and vertical directions, respectively. The $\rho(\cdot)$ is defined as

$$\rho(x) \begin{cases} -\theta_1 |x| & x \leq l_t \\ -(\theta_2 x^2 + \theta_3) & x > l_t \end{cases} \quad (27)$$

where l_t , θ_1 , θ_2 , and θ_3 are all fixed parameters. The sparse constraint is also imposed on the PSF h : $R_h(h) = \|h\|_1$. The detail of the algorithm used for solving the optimization problem (25) can be found in [41]. In our experiments, two types of parameter setting are used for the simulated data and the real data, respectively. In simulated experiments, “kernelWidth”, “kernelHeight”, “noiseStr”, and “deblurStrength” are set to 5, 5, 0.03, and 0.2, respectively; all other parameters use the default settings, and the description of all the parameters can be

found in [41]. For real sequences, setting the same parameters to $(7, 7, 0.03, 0.5)$ can reproduce the displayed results. Finally, we summarize the proposed atmospheric turbulence removal algorithm in Algorithm 2.

Algorithm 2: Atmospheric Turbulence Removal Algorithm

Input: Distorted image set $V \in \mathbb{R}^{w \times h \times n} = \{f_1, \dots, f_n\}$
Output: Restored image L

```

1  $u \leftarrow \text{Low\_Rank\_Decomposition}(V)$ ;
  // out_loop
2 while  $iter < iter\_max$  do
  // middle_loop
3   while  $\sum_i \|\Phi_i u - f_i\| > \varepsilon_1$  do
4     Initialize the  $\tilde{f}_i = f_i$ ;
5     Compute each  $\Phi_i$  which warps  $u$  to the observed image  $f_i$  using B-spline registration;
  // inner_loop
6     while  $\sum_i \|\Phi_i u - \tilde{f}_i\| > \varepsilon_2$  do
7        $v = u - \delta \sum_i \Phi_i^T (\Phi_i u - \tilde{f}_i)$ ;
8       Solve  $u = \text{argmin}_u \mu J(u) + \frac{1}{2\delta} \|u - v\|^2$  by iteration in Section 3.2;
9     end
10     $\tilde{f}_i \leftarrow \tilde{f}_i + f_i - \Phi_i u$ ;
11  end
12   $\hat{u} = u$ ;
13   $\{R_i\} \leftarrow$  register each frame  $f_i$  to  $\hat{u}$ ;
14   $V \leftarrow \{R_i\}$ ;
15   $u \leftarrow \text{Low\_Rank\_Decomposition}(V)$ ;
16 end
17 Construct single frame  $Z$  from  $\{R_i\}$  using Spatial-Temporal kernel regression in Section 4;
18 Deblur the image  $Z$  to get the latent sharp image  $L$  in Section 5;
19 Return  $L$ ;
```

VI. EXPERIMENTAL RESULTS AND ANALYSIS

This section presents extensive experimental validation of the proposed restoration method. We first show that low-rank decomposition improves the quality of the reference image compared to traditional methods. Next, we compare the results optimized using the proposed variational model to those using a spatial regularizer alone, to illustrate the advantages of our model. Finally, both qualitative and quantitative methods are used to evaluate the performance of the proposed method in comparison with several state-of-the-art methods. For quantitative evaluation, the *Peak Signal to Noise Ratio* (PSNR) and *Structural Similarity Index* (SSIM) are adopted to objectively evaluate the quality of the restored images.

For all the experiments, the intervals of the control points in the registration are set to $\varepsilon_x = \varepsilon_y = 16$ pixels, and the patch size L of r_k is set to 13. For non-local total variance, the local patch size is set to 5×5 (the support region for a certain pixel), the search window size is set to 21×21 (the region for searching for similar patches), and the

number of best neighbors is set to 10 (the number of accepted similar pixels in the search window). Moreover, for the number of optimized iterations (Algorithm 2 in Section V), $out_loop = 1$ is sufficient for all the test sequences and most of degradation cases, and the $middle_loop$ and $inner_loop$ are set to 3 and 10, respectively. Furthermore, in the variational model, the parameters λ_1 and λ_2 should satisfy the condition defined in Lemma 1 in Section VIII-B, so they are chosen to be equal: $\lambda_1 = \lambda_2 = 0.02$. With respect to the trade-off between spatial and temporal regularization, we choose $\mu_1 = 0.5$ and $\mu_2 = 0.25$. The proposed method is implemented in Matlab with MEX, and all the experiments are performed on a standard Intel Core i7 2.8GHz computer. The code and data of the proposed method are available at <https://sites.google.com/site/yuanxiehomepage/>.

We compare the proposed method with five representative algorithms: the lucky region method [16] (**Lucky region**), principal components analysis for atmospheric turbulence [11] (**PCA**), the data-driven two-stage approach for image restoration [42] (**Twostage**), Bregman iteration and non-local total variance for atmospheric turbulence stabilization [19] (**BNLTV**), and near-diffraction-limited-based image reconstruction for removing turbulence [7] (**NDL**). It is worth noting that the Twostage method was originally designed for recovering the true image of an underwater scene from a sequence distorted by water waves. Even though the medium is different, Twostage still achieves reasonable results on images distorted by air turbulence, and therefore the comparison and inclusion of this algorithm is valid. The respective authors provide the Twostage [42] and NDL [7] code, and the parameters remain unchanged. We have implemented the code for the other algorithms, which remains faithful to the original papers.

A. Quality of the Low-rank-based Reference Image

In this subsection we compare the visual quality of the reference images generated by our proposed method, temporal averaging, and the lucky region approach [16]. The reference images are presented in Fig. 7, where the first column (a) contains three observed frames from the 'chimney', 'airport', and 'city_strong' sequences; the other three columns are the results of temporal averaging (b), lucky-region (c), and low-rank decomposition (d), respectively. In the chimney sequence, the low-rank decomposed reference image is slightly sharper than the other two images. Nevertheless, due to the image being affected by only weak turbulence, the observed difference between the three reference images is small. However, in the case of severe turbulence (airport sequence), the effects are more noticeable. The magnified area of the region of interest (marked by the green box) can be seen in the lower right hand corner of each image. Low-rank decomposition produces sharp edges, while the images produced by temporal averaging and the lucky region methods remain blurred; similar results are seen in the city_strong sequence. In addition, the other methods produce heavy edge artifacts, *e.g.*, in the region of the bridge, with much sharper and clearer edges produced by our method, even in the case of relatively indistinct edges. These indistinct edges can subsequently be enhanced by using the variational model.

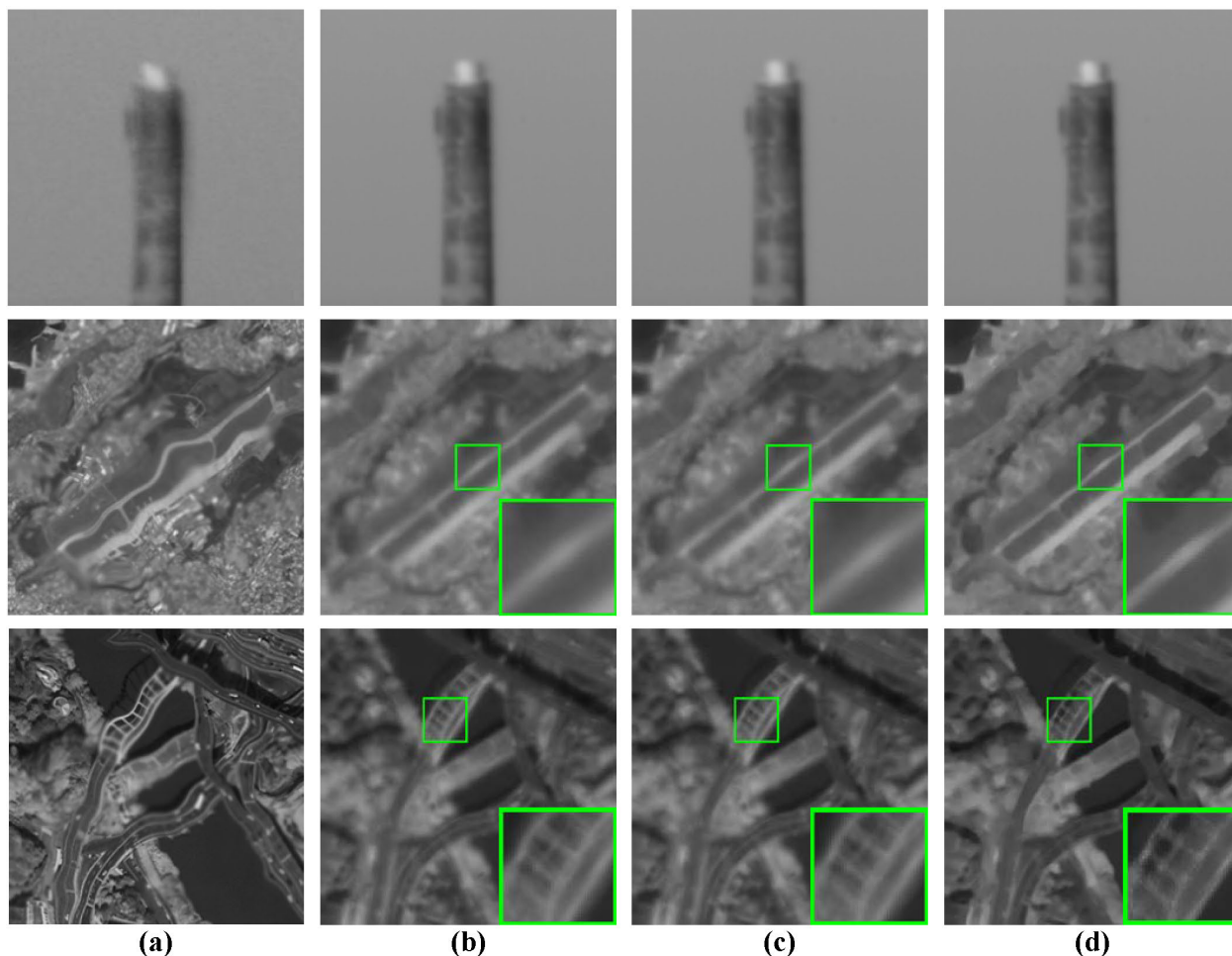


Figure 7. Comparison of the reference images constructed by three methods

B. Advantages of the Spatial-Temporal Regularization

This subsection illustrates the advantages of spatial-temporal regularization. We therefore compare the reference image u optimized using the two regularization terms: (1) the spatial-temporal regularizer as proposed; and (2) the spatial regularizer (traditional NLTV). Figs. 8 and 9 show the process of optimization using the two regularizers on the city_strong and airport sequences, respectively. Image (a) is the initial reference image obtained by low-rank decomposition, and the other three columns from left to right present the first, second, and the final optimization steps (the three steps correspond to the *middle_loop* in Algorithm 2).

As can be seen by comparing (a) with the bottom row of (d) in Fig. 8, the spatial regularizer enhances 'strong' edges (we refer to object's profile as the strong edges, and consider the edges which are inside an object to describe local structures as the weak edges), but the weak edges are not optimally recovered and remain blurry. In contrast, the spatial-temporal regularizer sharpens both strong and weak edges (top row Fig. 8). This phenomenon can be explained by the following two factors: 1) NLTV is limited by its preservation of texture and local structures in an

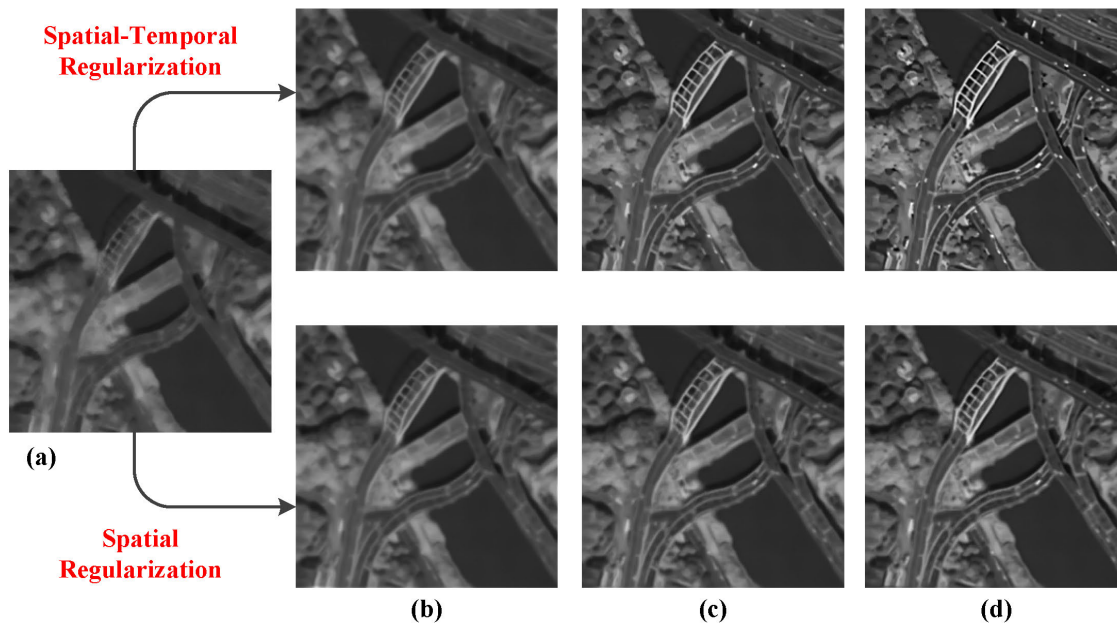


Figure 8. Optimization of the two regularizers for the city_strong sequence.

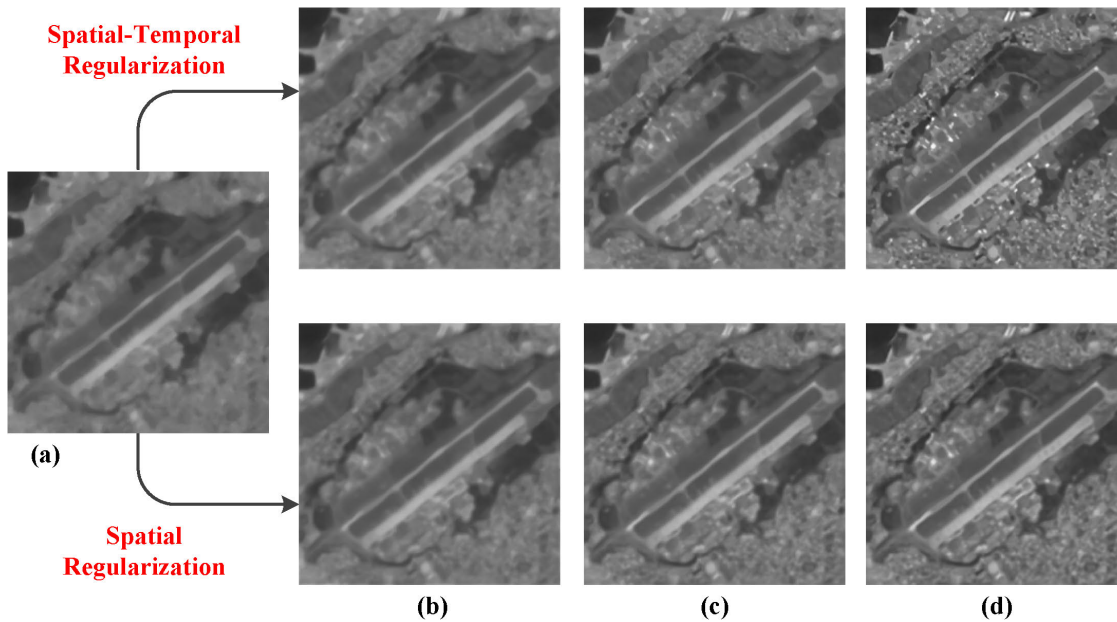


Figure 9. Optimization of the two regularizers for the airport sequence.

image due to the smoothness caused by the weighted averaging of non-local self-similar patterns. Unfortunately, these local structures usually include weak edges, resulting in different degrees of recovery of strong and weak edges. 2) The total variation employed by $J_t(u)$ can force the energy difference of two optimized results to converge on the sparse discontinuities, on which the edges lie in the functional space. Therefore, $J_t(u)$ can enhance both strong and weak edges. In summary, combining the non-local TV-based spatial regularizer with the local TV-based temporal regularizer does noticeably improve the quality of the reference image. More illustrative results can be seen in Fig. 9.

Additionally, we analyze the computational complexity and CPU time of the proposed fast algorithm and the split Bregman method (the iterative optimization algorithm is presented in Section VIII-A (from Eqs. (28) to (31)). For a fixed number of iterations, both the split Bregman method and our approach are linear in N (the number of pixels), since each step only contains addition and scalar multiplication operations. Therefore, we compare them in a different way by accounting for the number of atom operators in the key steps of each method, which in this case are Eqs. (14) and (28), respectively, because the complexity difference between $cut(\cdot)$ and $shrink(\cdot)$ is a constant. Considering one pixel access as an atom operator (ao), we can compare the complexity of the two methods in detail. ∇_x and ∇_x^T are both 2 aos , as are ∇_y and ∇_y^T . According to $\Delta = -\nabla_x^T \nabla_x - \nabla_y^T \nabla_y$, Δ is 8 aos . ∇_w , Δ_w and div_w are 20 aos if we choose ten similar patterns in NLTV. Therefore, solving Eq. (28) requires $86N$ aos , while Eq. (14) only requires 25 aos . So, for a large image or a large number of optimized iterations, the proposed algorithm can significantly reduce the computational time. Table I compares the split Bregman method and the proposed fast algorithm for solving the spatial-temporal regularizations in terms of the CPU seconds. The absence of PDEs leads to at least a one-quarter reduction in running time, and the proposed fast algorithm is therefore highly efficient.

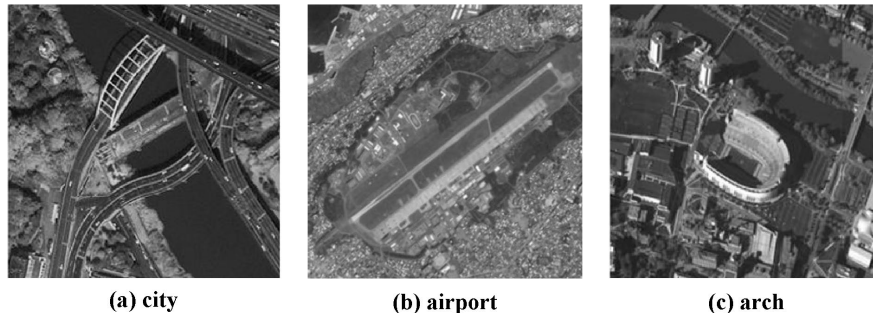


Figure 10. Three sharp images used in simulated experiments.

C. Simulated Experiments

To quantitatively evaluate the performance of the proposed method, we generated a set of simulated degraded sequences with different degrees of turbulence. The latent sharp images (260×260) are shown in Fig. 10. The simulation algorithm is similar to [7] but with a slight difference. The algorithm includes three key components: the deformation field, spatially variant PSFs, and a spatially-invariant diffraction-limited PSF. The deformation field

TABLE I
COMPARISON OF CPU TIME (AVERAGE) FOR THE SPLIT BREGMAN AND THE PROPOSED FAST ALGORITHM FOR DIFFERENTLY SIZED IMAGES

	240 × 240	260 × 260	320 × 240
Split Bregman	0.6496	0.6231	1.1588
Proposed	0.4482	0.4693	0.7805
Reduction	31.00%	24.68%	32.65%

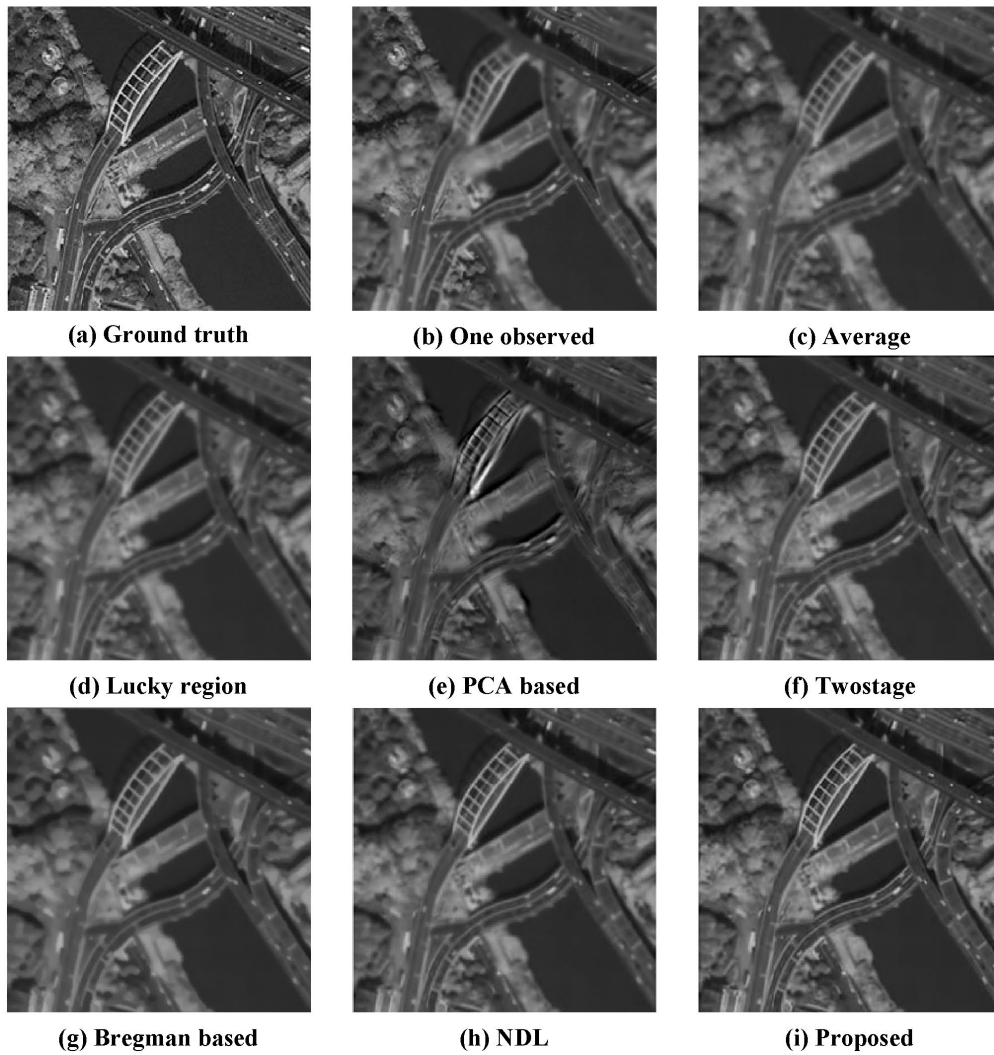


Figure 11. Image restoration results on the simulated city_weak sequence.

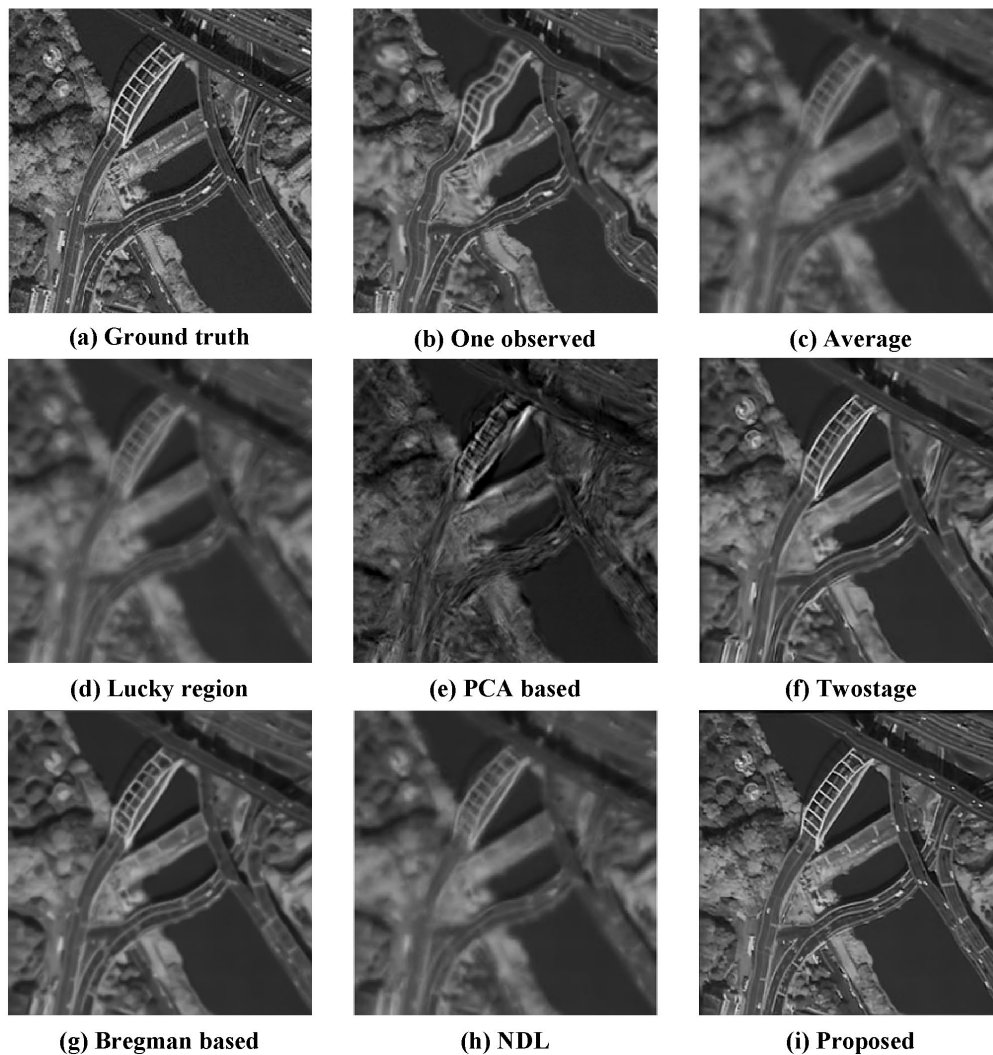


Figure 12. Image restoration results on the simulated city_strong sequence.

is determined by a set of control points whose random offsets have a Gaussian distribution with mean $\mu_d = 0$ and variance σ_d^2 , with σ_d^2 indicating the turbulence strength. The space-varying blur is generated by convolution with a set of PSFs, each of which is also a Gaussian function with variance proportional to the magnitude of the corresponding local motion energy. In our implementation, the number of control points is characterized by their interval d_g , and the number of PSFs is equal to the number of control points. To efficiently apply a spatially-variant blur, we use the fast algorithm described in [43], which is based on overlap-add convolution schemes [44] and linear interpolation of measured PSFs for spatially-invariant blurs. The spatially-invariant diffraction-limited blur is produced using a disc function.

To test the performance of the different restoration methods with different degrees of turbulence, we produced two degraded sequences for the same true image (Fig. 10 (a)) named city_weak and city_strong, respectively. Considering limited page length, we only simulate two kinds of turbulence for one image (city); the other two images are used

TABLE II
COMPARISON OF PSNR AND SSIM OBTAINED BY DIFFERENT METHODS

<i>Sequence</i>	Average	Lucky-Region	PCA Based	Twostage	BNLTV	NDL	Proposed
Airport	69.7747	69.7758	66.7340	68.7511	69.3926	68.3036	69.9754
	0.2745	0.2731	0.2042	0.2566	0.3830	0.3520	0.4011
City_strong	68.2606	66.9073	63.2749	66.4798	67.0916	68.6392	67.4820
	0.2479	0.2405	0.1329	0.2378	0.3413	0.2854	0.3544
City_weak	68.8989	67.3415	64.8207	67.4399	67.3981	68.9629	68.7218
	0.3611	0.3531	0.2215	0.2686	0.3631	0.3956	0.4022
Architecture	70.2634	68.1599	64.1939	68.8656	68.3711	67.9243	70.5919
	0.4299	0.4282	0.2929	0.3656	0.4349	0.4340	0.5851
Chimney	78.9262	79.1731	64.4229	78.7460	75.0367	79.5622	79.9611
	0.1194	0.1137	0.0539	0.1193	0.1120	0.1075	0.1257
Building	72.1991	72.1987	62.4768	73.2032	72.9388	74.3453	74.3843
	0.3201	0.3271	0.1858	0.3882	0.3855	0.4857	0.5023

to produce the airport sequence with strong turbulence and the arch sequence with weak turbulence, respectively. The parameter configuration for the two cases are listed as follows: for weak turbulence, $\sigma_d^2 = 4$, $d_g = 32$, and the variance of the added Gaussian noise $\sigma_n^2 = 3$; for strong turbulence, $\sigma_d^2 = 10$, $d_g = 16$, and the variance of the added Gaussian noise $\sigma_n^2 = 16$. Table II compares the PSNR and SSIM values for all the outputs of the seven different restoration algorithms. Each sequence has two sub rows, the top one denoting the PSNR values, and the bottom one denoting the SSIM values.

The restoration results of the city_weak sequence are illustrated in Fig. 11. The lucky region method (Fig. 11 (d)) does not seem to offer an improvement over the mean image (Fig. 11 (c)). The PCA-based method produces unnatural components due to the loss of high frequency information. BNLTV restores the structure of the objects well but cannot recover local details. This is due in large part to the smoothness caused by the weighted averaging of non-local self-similar patterns. Consequently, the smoothness prevents the restoration algorithm from recovering the local details. Twostage and NDL achieve similar results (Figs. 11 (f) and (h)); the distortion has been corrected thoroughly but some blur still exists. The proposed approach significantly improves visual quality and recovers many high-frequency details in the image. Even more noticeable differences are shown in Fig. 12, depicting the results of the city_strong sequence with severe turbulence (see one of the observed frames in Fig. 12 (b)). Twostage and BNLTV are superior to NDL, as shown in Fig. 12 (h), which produces many artifacts. Only the proposed method can remove large deformations and simultaneously recover detail. The superiority of the proposed algorithm is due to the high-quality reference image and its subsequently optimized version facilitating the removal of distortion, and the spatial-temporal kernel regression recovering sharp local details as well as reducing the noise introduced by the sensor and the registration error. More experimental results are shown in Fig. 13 and Fig. 1 in the Appendix.

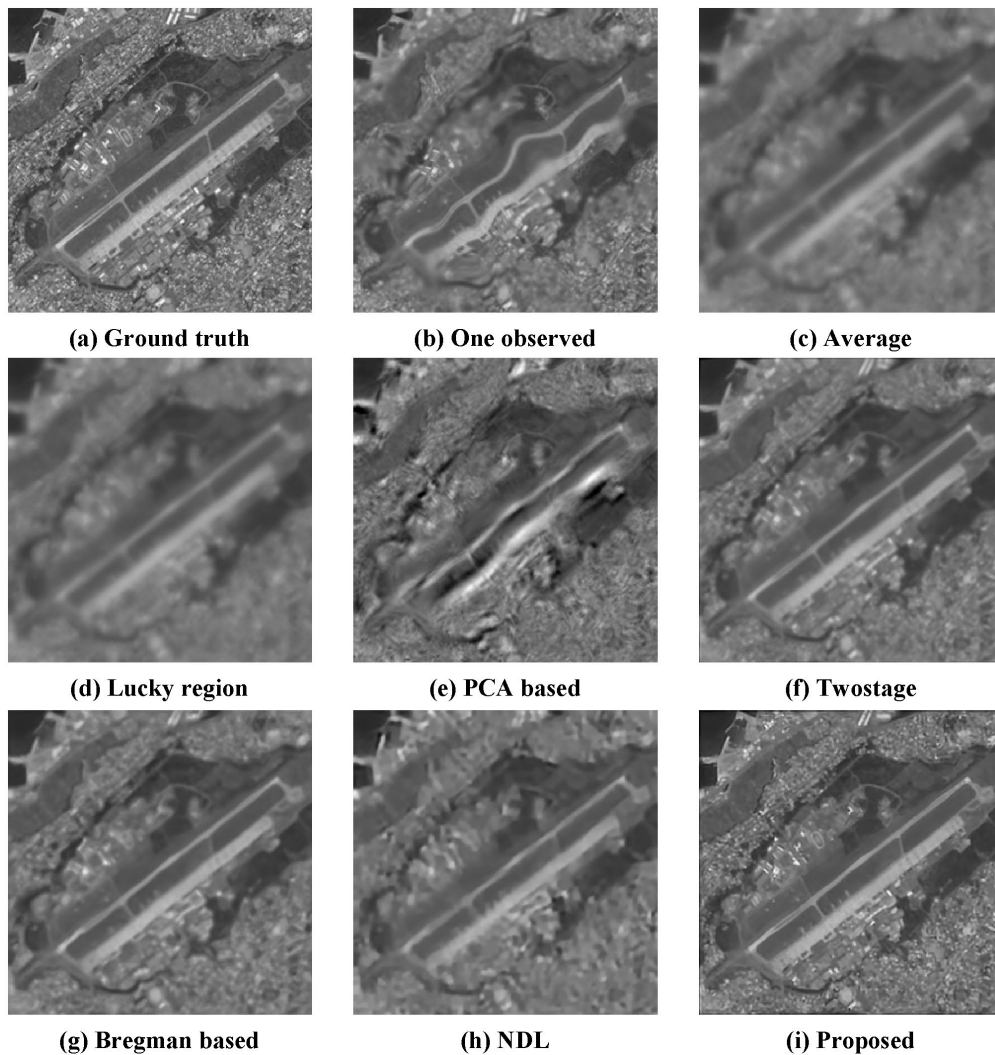


Figure 13. Image restoration results on the simulated airport sequence.

D. Real Video Experiments

We test several video sequences captured through real atmospheric turbulence to illustrate the performance of the proposed restoration algorithm. In the first sequence, a chimney is captured through hot air exhausted by a building's vent (the original size of the videos 'chimney' and 'building' is $237 \times 237 \times 100$; we resize them to $240 \times 240 \times 100$ in order to facilitate non-rigid registration). The final outputs of all the methods are shown in Fig. 14: the proposed algorithm provides the best restoration result and faithfully recovers details of the object. The PSNR and SSIM values also indicate that the proposed method outperforms the other methods for the chimney sequence. A noteworthy phenomenon is that all the PSNR values of the average outputs are relatively high (shown in Table II), because PSNR is known to sometimes correlate poorly with human perception [45].

Similar restoration results are seen in the experiment on the second test sequence, 'building' ($240 \times 240 \times 100$). Most restoration methods cannot remove diffraction-limited blur, except for NDL and our algorithm. Both of these

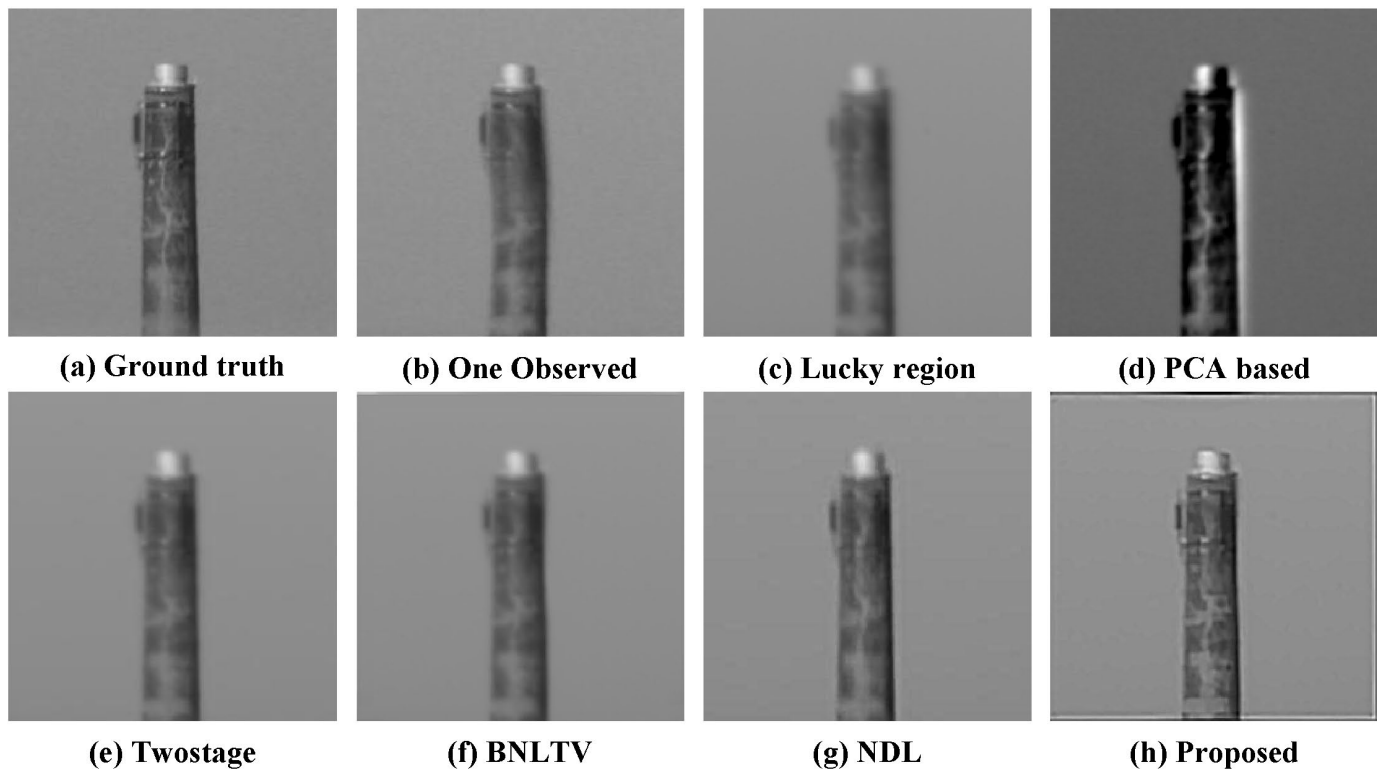


Figure 14. Image restoration results on the chimney sequence.

methods can produce sharp restored images, but the NDL output (Fig. 15 (g)) contains halo artifact near the edges, such as around the windows of the building. Such artifacts can be attributed to the limited accuracy of the PSF estimation and the existence of noise caused by sensor and registration error. As mentioned earlier, NDL and the proposed method utilize the same deconvolution algorithm with identical parameters to produce the final outputs. Since the major cause of artifact appears to be noise, we can conclude that the noise can be effectively reduced by spatial-temporal kernel regression. More real data experimental results are presented in the Appendix.

VII. DISCUSSION AND CONCLUSIONS

In this paper, we propose a new method to restore a high-quality image from a given image sequence degraded by atmospheric turbulence. Geometric distortion and space-time-varying blur are the major challenges that need to be overcome during restoration. To effectively remove local distortion, the proposed method constructs a high-quality reference image using low-rank decomposition. Then, to further improve the registration, the proposed method applies a variational model with a novel spatial-temporal regularization term to iteratively optimize the reference image; the proposed fast algorithm can efficiently solve this variational model. To reduce blur variation, the registered frames can be fused into a single image with reduced PSF variation by applying near-stationary patch detection and distortion-driven spatial-temporal kernel regression. The fused image can be deblurred by a space-invariant blind deconvolution method in order to produce the final output. Thorough empirical studies on a

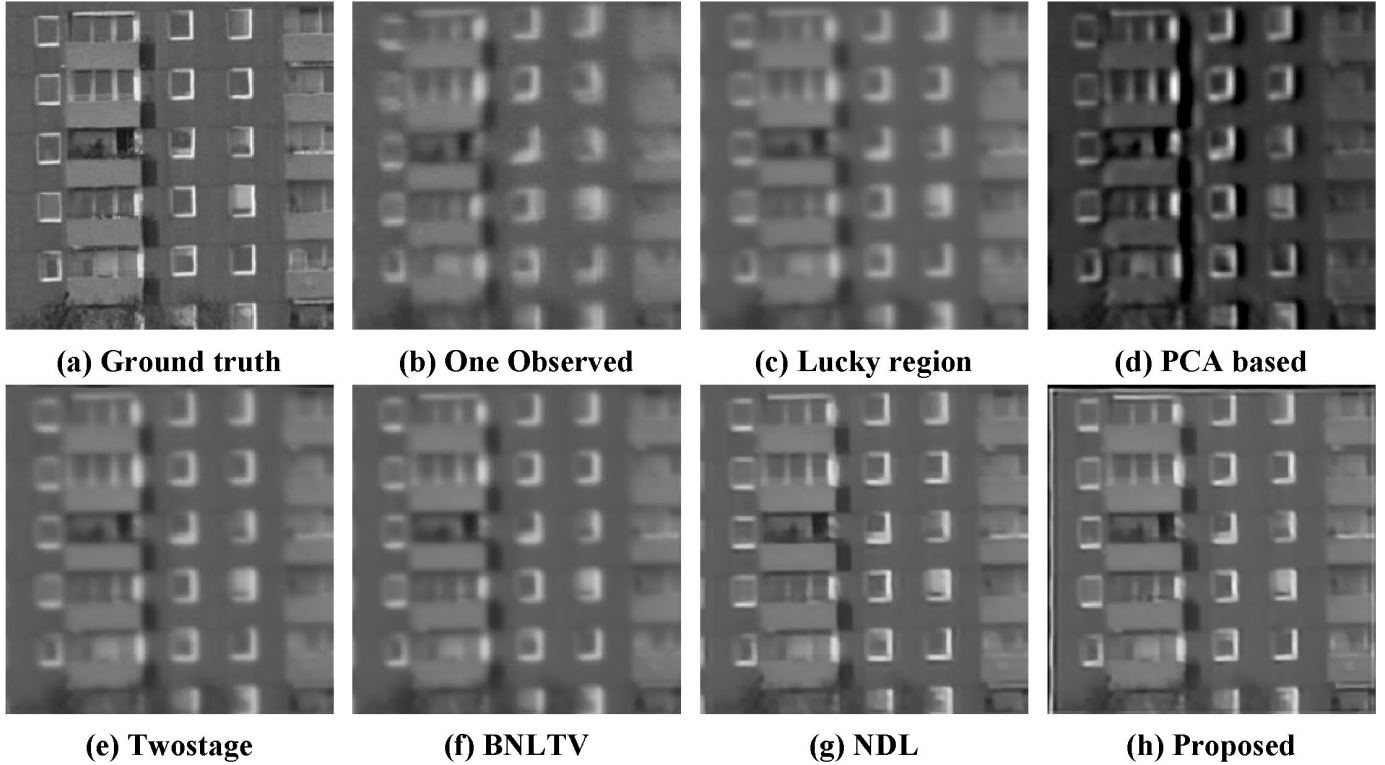


Figure 15. Image restoration results on the building sequence.

set of simulated data and real videos demonstrate the effectiveness and the efficiency of the new framework for recovering a single image from a degraded sequence.

Additionally, we test the performance of the proposed restoration method on images distorted by water rather than air (see the Appendix in supplemental material), with promising results. This method is therefore suitable for use with multiple distorting media, although further adaptations of the proposed method are likely.

VIII. PROOF

A. Split Bregman for Solving Mixed ROF Model

The split Bregman method for solving the mixed ROF subproblem (10) is presented below:

Let $b_w^0 = 0, b_x^0 = 0, b_y^0 = 0$ and $u^0 = v$, for $k = 1, 2, \dots$, the iteration is as follows

$$u^{k+1} = (I - 2\lambda_1 \Delta_w - \lambda_2 \Delta)^{-1} (v + \lambda_1 \operatorname{div}_w (b_w^k - d_w^k) + \lambda_2 \nabla_x^T (d_x^k + \nabla_x u_p - b_x^k) + \lambda_2 \nabla_y^T (d_y^k + \nabla_y u_p - b_y^k)) \quad (28)$$

$$d_w^{k+1} = \operatorname{shrink} \left(\nabla_w u^{k+1} + b_w^k, \frac{\mu_1}{\lambda_1} \right) \quad (29)$$

$$d_x^{k+1} = \operatorname{shrink} \left(\nabla_x u^{k+1} - \nabla_x u_p + b_x^k, \frac{\mu_2}{\lambda_2} \right) \quad (30)$$

$$d_y^{k+1} = \operatorname{shrink} \left(\nabla_y u^{k+1} - \nabla_y u_p + b_y^k, \frac{\mu_2}{\lambda_2} \right) \quad (31)$$

where ∇_x and ∇_y are the difference operators along the x and y directions, respectively, $\Delta := -\nabla_x^T \nabla_x - \nabla_y^T \nabla_y$ is the discrete Laplacian operator, ∇_w denotes the non-local gradient operator and Δ_w represents the non-local graph Laplacian, and div_w is the non-local graph divergence operator (see the mathematical definitions of all those operators in Appendix). Moreover, the function $\text{shrink}(\cdot, \cdot)$ is defined as:

$$\text{shrink}(x, \gamma) = \frac{x}{|x|} * \max(|x| - \gamma, 0) \quad (32)$$

B. Proof of Theorem 1

The detailed proof of the theorem 1 is given below.

Lemma 1. *Given $0 < 20\lambda_1 + 4\lambda_2 < 1$, the real symmetric linear operator $I + 2\lambda_1\Delta_w + \lambda_2\Delta$ is positive definite.*

Lemma 2. *For $k = 1, 2, \dots$, let $d_w^k, d_x^k, d_y^k, b_w^k, b_x^k, b_y^k$ and u^{k+1} be given by the iteration (11) to (14). Then $\lim_{k \rightarrow \infty} (u^{k+1} - u^k) = 0$, and*

$$\begin{aligned} b_w^k &= \text{cut}(\nabla_w u^k + b_w^{k-1}, \frac{\mu_1}{\lambda_1}) \\ b_x^k &= \text{cut}(\nabla_x u^k - \nabla_x u_p + b_x^{k-1}, \frac{\mu_2}{\lambda_2}) \\ b_y^k &= \text{cut}(\nabla_y u^k - \nabla_y u_p + b_y^{k-1}, \frac{\mu_2}{\lambda_2}) \end{aligned}$$

Lemma 3. *For $k = 1, 2, \dots$, let $d_w^k, d_x^k, d_y^k, b_w^k, b_x^k, b_y^k$ and u^{k+1} be given by the iteration (11) to (14). Then all the sequences $(d_w^k)_{k=1,2,\dots}, (d_x^k)_{k=1,2,\dots}, (d_y^k)_{k=1,2,\dots}, (b_w^k)_{k=1,2,\dots}, (b_x^k)_{k=1,2,\dots}, (b_y^k)_{k=1,2,\dots}$ and $(u^k)_{k=1,2,\dots}$ are bounded. Moreover,*

$$u^{k+1} = v + \frac{\lambda_1}{\mu_1} \text{div}_w b_w^k - \frac{\lambda_2}{\mu_2} (\nabla_x^T b_x^k + \nabla_y^T b_y^k)$$

Lemma 4. *For $k = 1, 2, \dots$, let $d_w^k, d_x^k, d_y^k, b_w^k, b_x^k, b_y^k$ and u^{k+1} be given by the iteration (11) to (14). Then*

$$\begin{aligned} \lim_{k \rightarrow \infty} (d_w^k - \nabla_w u^k) &= 0 \\ \lim_{k \rightarrow \infty} (d_x^k - \nabla_x (u^k - u_p)) &= 0 \\ \lim_{k \rightarrow \infty} (d_y^k - \nabla_y (u^k - u_p)) &= 0 \end{aligned}$$

The proofs of the above lemmas are given in Appendix in supplemental material.

Theorem 1. *For $k = 1, 2, \dots$, let b_w^k, b_x^k, b_y^k and u^{k+1} be given by the iteration (11) to (14). If $0 < 20\lambda_1 + 4\lambda_2 < 1$, then $\lim_{k \rightarrow \infty} u^k = u^*$.*

Proof: Let $F(u) := (1/2)\|u - v\|_2^2$, then $\partial F(u) = u - v$. For $w \in \mathbb{R}^{N^2}$ we can get

$$F(u^{k+1} + w) - F(u^{k+1}) - \langle u^{k+1} - v, w \rangle \geq 0 \quad (33)$$

From Lemma 3, we have $-(u^{k+1} - v) = \frac{\lambda_2}{\mu_2} \nabla_x^T b_x^k + \frac{\lambda_2}{\mu_2} \nabla_y^T b_y^k - \frac{\lambda_1}{\mu_1} \text{div}_w b_w^k$, and moreover $\langle \text{div}_w p, q \rangle = -\langle p, \nabla_w q \rangle$. Then,

$$F(u^{k+1} + w) - F(u^{k+1}) + \langle \frac{\lambda_2}{\mu_2} b_x^k, \nabla_x w \rangle + \langle \frac{\lambda_2}{\mu_2} b_y^k, \nabla_y w \rangle + \langle \frac{\lambda_1}{\mu_1} b_w^k, \nabla_w w \rangle \geq 0 \quad (34)$$

Recall that $G(d) = \|d\|_1$, $\frac{\lambda_1}{\mu_1} b_w^k \in \partial G(d_w^k)$, $\frac{\lambda_2}{\mu_2} b_x^k \in \partial G(d_x^k)$ and $\frac{\lambda_2}{\mu_2} b_y^k \in \partial G(d_y^k)$, so,

$$\|d_w^k + \nabla_w w\|_1 - \|d_w^k\|_1 - \langle \frac{\lambda_1}{\mu_1} b_w^k, \nabla_w w \rangle \geq 0 \quad (35)$$

$$\|d_x^k + \nabla_x w\|_1 - \|d_x^k\|_1 - \langle \frac{\lambda_2}{\mu_2} b_x^k, \nabla_x w \rangle \geq 0 \quad (36)$$

$$\|d_y^k + \nabla_y w\|_1 - \|d_y^k\|_1 - \langle \frac{\lambda_2}{\mu_2} b_y^k, \nabla_y w \rangle \geq 0 \quad (37)$$

Adding (34) ~ (37) gives

$$\|d_w^k\|_1 + \|d_x^k\|_1 + \|d_y^k\|_1 + F(u^{k+1}) \leq \|d_w^k + \nabla_w w\|_1 + \|d_x^k + \nabla_x w\|_1 + \|d_y^k + \nabla_y w\|_1 + F(u^{k+1} + w) \quad (38)$$

Suppose that $(k_j)_{j=1,2,\dots}$ is an increasing sequence of positive integers such that the sequence $(u^{k_j})_{j=1,2,\dots}$ converges to the limit \tilde{u} . By Lemma 2, we have $\lim_{k \rightarrow \infty} (u^{k+1} - u^k) = 0$. Therefore, $\lim_{j \rightarrow \infty} u^{k_j+1} = \tilde{u}$. Moreover, we have the following via the Lemma 4:

$$\lim_{j \rightarrow \infty} d_w^k = \lim_{j \rightarrow \infty} [(d_w^k - \nabla_w u^k) + \nabla_w u^k] = \nabla_w \tilde{u} \quad (39)$$

also have

$$\lim_{j \rightarrow \infty} d_x^k = \lim_{j \rightarrow \infty} [(d_x^k - \nabla_x (u^k - u_p)) + \nabla_x (u^k - u_p)] = \nabla_x (\tilde{u} - u_p) \quad (40)$$

$$\lim_{j \rightarrow \infty} d_y^k = \lim_{j \rightarrow \infty} [(d_y^k - \nabla_y (u^k - u_p)) + \nabla_y (u^k - u_p)] = \nabla_y (\tilde{u} - u_p) \quad (41)$$

Replacing k by k_j in (38) and let $j \rightarrow \infty$, we have:

$$\begin{aligned} \|\nabla_w \tilde{u}\|_1 + \|\nabla_x (\tilde{u} - u_p)\|_1 + \|\nabla_y (\tilde{u} - u_p)\|_1 + F(\tilde{u}) &\leq \|\nabla_w (\tilde{u} + w)\|_1 + \\ &\|\nabla_x (\tilde{u} - u_p + w)\|_1 + \|\nabla_y (\tilde{u} - u_p + w)\|_1 + F(\tilde{u} + w) \end{aligned}$$

The above equations hold for all the $w \in \mathbb{R}^{N^2}$. On the other hand, u^* is the unique solution to the minimization problem (10). Therefore, we must have $\tilde{u} = u^*$. Since $(u^k)_{k=1,2,\dots}$ is a bounded sequence, we have

$$\lim_{k \rightarrow \infty} u^k = u^*. \quad (42)$$

This completes the proof of the Main Theorem 1. ■

REFERENCES

- [1] Y. Yitzhaky, I. Dror, N. S. Kopeika. Restoration of atmospherically blurred images according to weather-predicted atmospheric modulation transfer functions. *Optical Engineering*, 3064-3072(36), 1997.
- [2] J. E. Pearson. Atmospheric turbulence compensation using coherent optical adaptive techniques. *Applied Optics*, 622-631(15), 1976.
- [3] K. T. Robert. Adaptive optics compensation of atmospheric turbulence: the past, the present, and the promise. *Proceedings of SPIE, Atmospheric Propagation and Remote Sensing III*, 404-412(2222), 1994.

- [4] M. A. Vorontsov. Parallel image processing based on an evolution equation with anisotropic gain: integrated optoelectronic architectures. *Journal of the Optical Society of America A*, 1623-1637(16), 1999.
- [5] M. A. Vorontsov, G. W. Carhart. Anisoplanatic imaging through turbulent media: image recovery by local information fusion from a set of short-exposure images. *Journal of the Optical Society of America A*, 1312-1324(18), 2001.
- [6] X. Zhu, P. Milanfar. Image Reconstruction from videos distorted by atmospheric turbulence. *Proceedings of SPIE*, 2010.
- [7] X. Zhu, P. Milanfar. Removing atmospheric turbulence via space-invariant deconvolution. *IEEE Trans. on Pattern Analysis and Machine Intelligence*, 157-170(35), 2013.
- [8] M. Shimizu, S. Yoshimura, M. Tanaka, M. Okutomi. Super-resolution from image sequence under influence of hot-air optical turbulence. *Computer Vision and Pattern Recognition*, 2008.
- [9] M. Hirsch, S. Sra, B. Schölkopf, S. Harmeling. Efficient filter flow for space-variant multiframe blind deconvolution. *IEEE Conference on Computer Vision and Pattern Recognition*, 607-614, 2010.
- [10] N. M. Law. Lucky imaging: Diffraction-limited astronomy from the ground in the visible. *Ph.D. Thesis, Cambridge University*, 2003.
- [11] D. Li, R. M. Mersereau, S. Simske. Atmospheric turbulence-degraded image restoration using principal components analysis. *IEEE Geoscience and Remote Sensing Letters*, 340-344(4), 2007.
- [12] M. C. Roggemann, C. A. Stoudt, B. M. Welsh. Image-spectrum signal-to-noise-ratio improvements by statistical frame selection for adaptive-optics imaging through atmospheric turbulence. *Optical Engineering*, 3254-3264(33), 1994.
- [13] D. L. Fried. Probability of getting a lucky short-exposure image through turbulence. *Journal of the Optical Society of America A*, 1651-1658(68), 1978.
- [14] M. Aubailly, M. A. Vorontsov, G. W. Carhart, M. T. Valley. Image enhancement by local information fusion with pre-processing and composed metric. *Proceedings of SPIE*, 2008.
- [15] S. John, M. A. Vorontsov. Multiframe selective information fusion from robust error estimation theory. *IEEE Trans. on Image Processing*, 577-584(14), 2005.
- [16] M. Aubailly, M. A. Vorontsov, G. W. Carhart, M. T. Valley. Automated video enhancement from a stream of atmospherically-distorted images: the lucky-region fusion approach. *Proceedings of SPIE*, 2009.
- [17] S. Gepshtein, A. Shtainman, B. Fishbain, L. Yaroslavsky. Restoration of atmospheric turbulent video containing real motion using filtering and elastic image registration. *Proceeding of the Eusipco*, 2004.
- [18] D. Frakes, J. Monaco, M. Smith. Suppression of atmospheric turbulence in video using an adaptive control grid interpolation approach. *IEEE International Conference on Acoustics, Speech and Signal Processing*, 1881-1884(3), 2001.
- [19] Y. Mao, J. Gilles. Nonrigid geometric distortions correction - Application to atmospheric turbulence stabilization. *Inverse Problems and Imaging*, 531-546(6), 2012.
- [20] J. Gilles, T. Dagobert, C. D. Franchis. Atmospheric turbulence restoration by diffeomorphic image registration and blind deconvolution. *Proceedings of Advanced Concepts for Intelligent Vision Systems*, 400-409, 2008.
- [21] E. J. Candes, X. Li, Y. Ma, J. Wright. Robust principal component analysis? *Journal of ACM*, 1-37, 58(1), 2009
- [22] D. Rueckert, L. Sonoda, C. Hayes, D. Hill, M. Leach, D. Hawkes. Nonrigid registration using free-form deformations: application to breast mr images. *IEEE Trans. on Medical Imaging*, 712-721, 18(8), 1999.
- [23] A. Myronenko, X. Song. Intensity-based image registration by minimizing residual complexity. *IEEE Trans. on Medical Imaging*. 1882-1891(29), 2010.
- [24] L. Bregman. The relaxation method of finding the common points of convex sets and its application to the solution of problems in convex optimization. *USSR Computational Mathematics and Mathematical Physics*, 200-217(7), 1967.
- [25] S. Osher, M. Burger, D. Goldfarb, J. Xu, W. Yin. An iterative regularization method for total variation-based image restoration. *SIAM Journal on Multiscale Modeling and Simulation*, 460-489(4), 2005.
- [26] J. Xu, S. Osher. Iterative regularization and nonlinear inverse scale space applied to wavelet-based denoising. *IEEE Trans. on Image Processing*, 534-544(16), 2006.
- [27] L. He, T. C. Chang, S. Osher, T. Fang, P. Speier. MR image reconstruction by using the iterative refinement method and nonlinear inverse scale space methods. *UCLA CAM Report*, 06-35, 2006.
- [28] X. Zhang, M. Burger, X. Bresson, S. Osher. Bregmanized nonlocal regularization for deconvolution and sparse reconstruction. *SIAM Journal on Imaging Sciences*, 253-276(3), 2010.

- [29] X. Zhang, M. Burger, S. Osher. A unified primal-dual algorithm framework based on Bregman iteration. *Journal of Scientific Computing*, 1–27(46), 2010.
- [30] P. Lions, B. Mercier. Splitting algorithm for the sum of two nonlinear operators. *SIAM Journal on Numerical Analysis*, 964–979(16), 1979.
- [31] PL. Combettes, VR. Wajs. Signal recovery by proximal forward-backward splitting. *Multiscale Modeling and Simulation*, 1168–1200, 2005.
- [32] G. B. Passty. Ergodic convergence to a zero of the sum of monotone operators in Hilbert space. *Journal of Mathematical Analysis and Applications*, 383–390(72), 1979.
- [33] L. I. Rudin, S. Osher, E. Fatemi. Nonlinear total variation based noise removal algorithm. *Journal of Physics D: Applied Physics*, 259–268(60), 1992.
- [34] D. Goldfarb, W. Yin. Parametric maximum flow algorithm for fast total variation minimization. *CAAM Technical report*, 2007.
- [35] T. Goldstein, S. Osher. The split Bregman method for L1-regularized problems. *SIAM Journal on Imaging Sciences*, 323–343(2), 2009.
- [36] R. Jia, H. Zhao. A fast algorithm for the total variation model of image denoising. *Advances in Computational Mathematics*, 231–241(33), 2010.
- [37] M. P. Wand, M. C. Jones. Kernel smoothing. *Series Monographs on Statistics and Applied Probability*, Chapman and Hall, 1995.
- [38] E. A. Nadaraya. On estimating regression. *Theory of Probability and Its Application*, 141–142, 1964.
- [39] H. Takeda, S. Farsiu, P. Milanfar. Kernel regression for image processing and reconstruction. *IEEE Trans. Image Processing*, 349–366(16), 2007.
- [40] T. Kato, S. Omachi, H. Aso. Asymmetric gaussian and its application to pattern recognition. *Proceedings of the Joint IAPR International Workshop on Structural, Syntactic, and Statistical Pattern Recognition*, 405–413, 2002.
- [41] Q. Shan, J. Jia, A. Agarwala. High-quality motion deblurring from a single image. *ACM Trans. Graphics*, vol. 27, 2008.
- [42] O. Oreifej, G. Shu, T. Pace, M. Shah. A two-stage reconstruction approach for seeing through water. *Computer Vision and Pattern Recognition*, 1153–1160, 2011.
- [43] J. G. Nagy, D. P. O’leary. Fast iterative image restoration with a space-varying PSF. *Advanced Signal Processing Algorithms, Architectures, and Implementations IV*, 388–399, 1997.
- [44] T. Stockham Jr. High-speed convolution and correlation. *ACM Spring Joint Computer Conference*, 229–233, 1966.
- [45] W. Xue, L. Zhang, X. Mou, A. C. Bovik. Gradient magnitude similarity deviation: a highly efficient perceptual image quality index. *arXiv:1308.3052*, 2013.

Appendix

Yuan Xie, *Member, IEEE*, Wensheng Zhang, Dacheng Tao, *Senior Member, IEEE*, Wenrui Hu,
Yanyun Qu, Hanzi Wang, *Senior Member, IEEE*,

I. ADDITIONAL EXPERIMENTS RESULTS

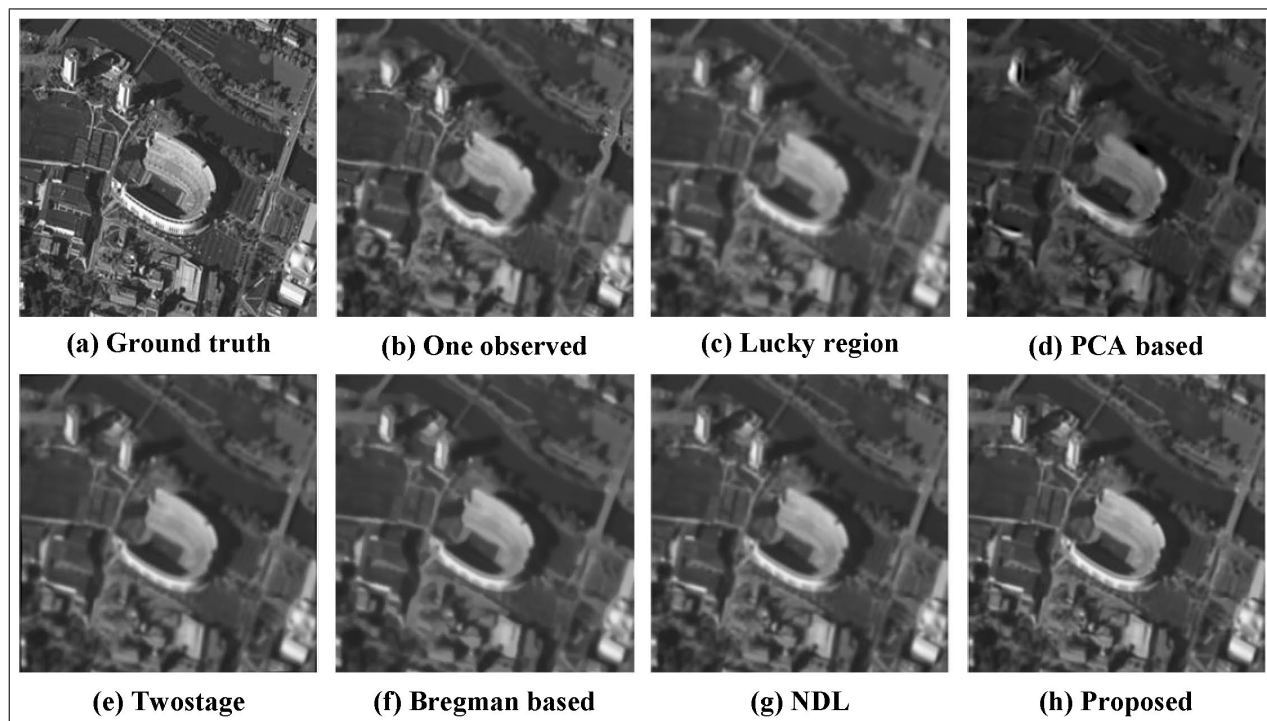


Figure 1. Image restoration results on simulated Arch sequence.

Another test sequence watertower shows the effect of severe turbulence during a hot summer day¹. As shown in Fig. 2 (a) and (b), each frame (320×240) of the video is quite noisy and highly blurred since the video is captured by long exposure. 100 frames are taken from the original video (285 frames), so the video for test is $320 \times 240 \times 100$. The lucky region, Twostage and BNLTV achieve similar results where the deformation and noise are well removed but severe blur still exists (Figs. 2 (c), (e) and (f)). Only the NDL and the proposed method can give significantly improvement in visual quality. However, compared with NDL (Fig. 2 (g)), the proposed method has done a bit better in handling the diffraction-limited blur (Fig. 2 (h)). Since we do not have the latent sharp image of watertower sequence, the quantitative evaluation can not be provided.

¹This video sequence can be downloaded from the website <http://www.iol.umd.edu/Movies/alot.php>.

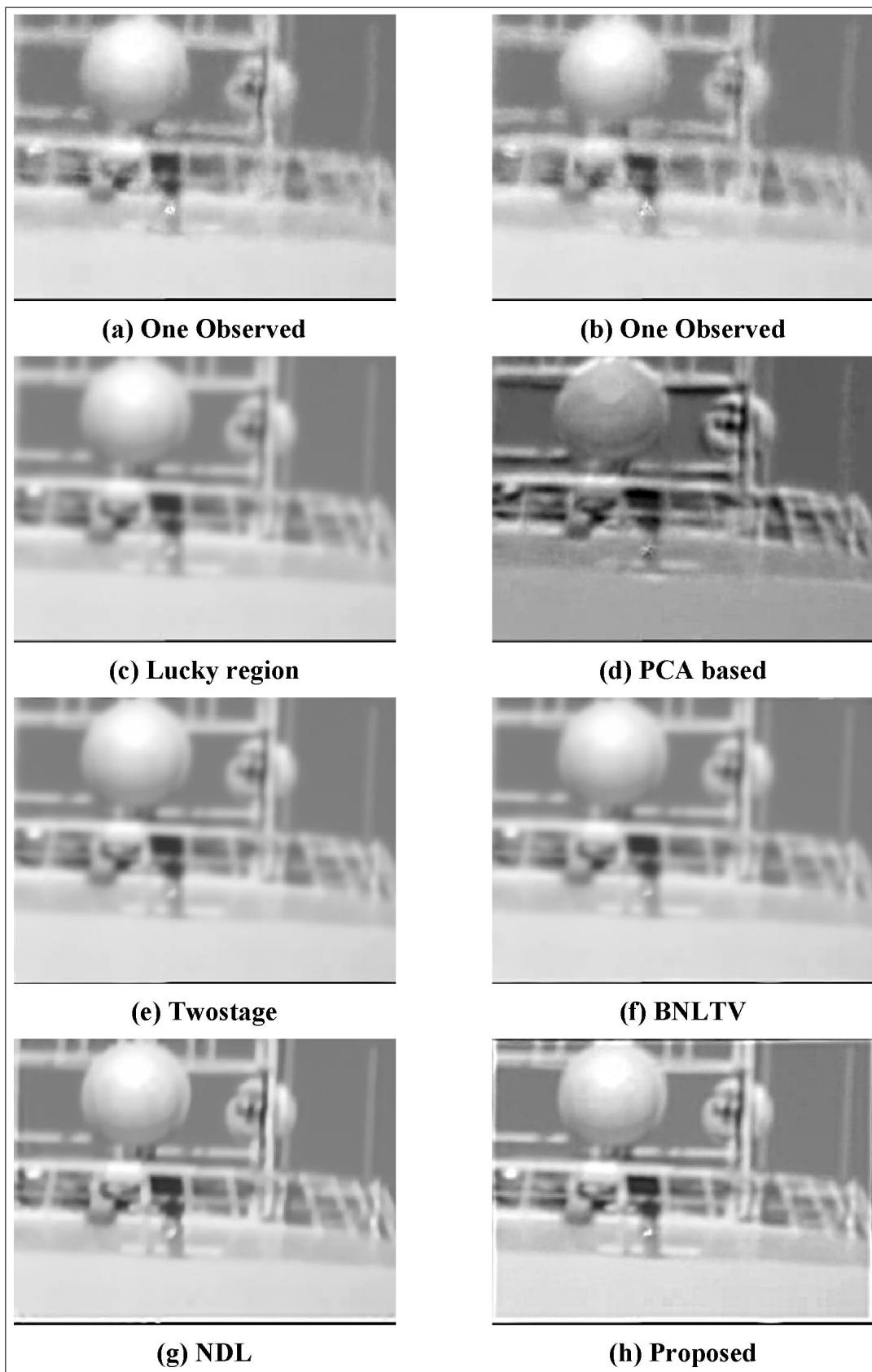


Figure 2. Image restoration results on Watertower sequence.

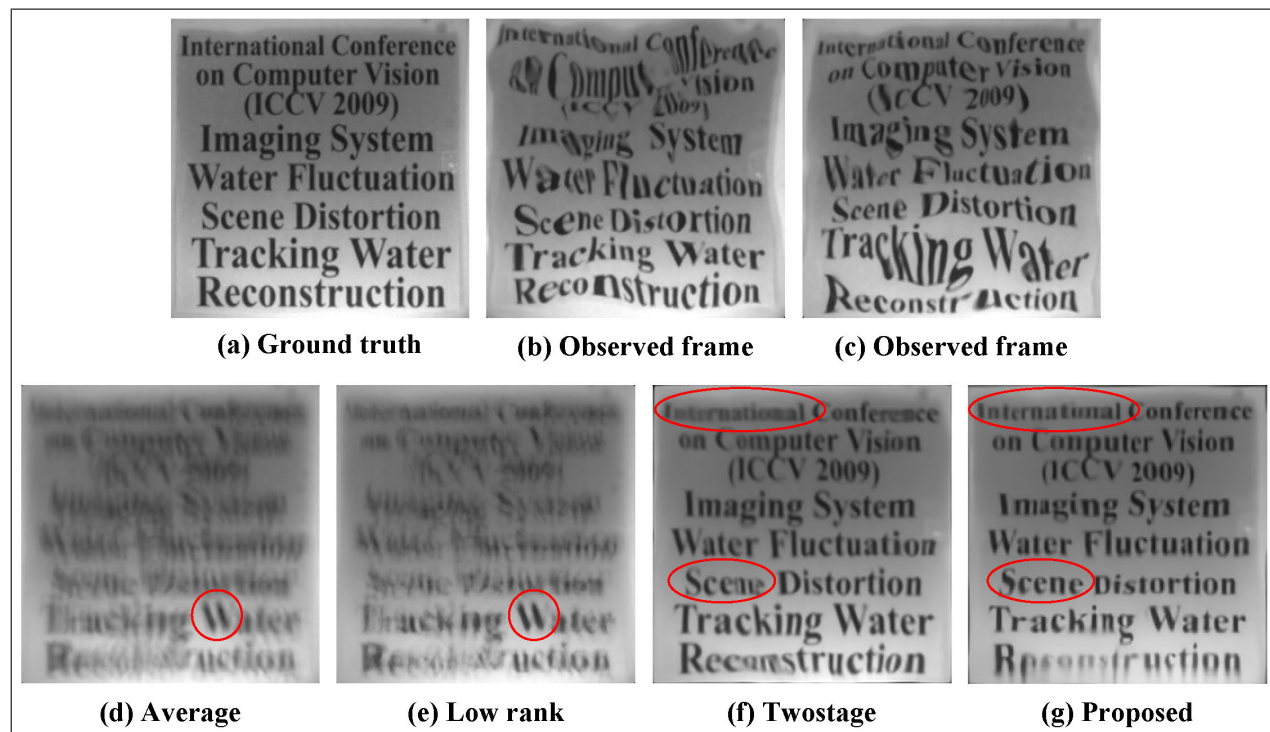


Figure 3. Image restoration results on standard underwater sequence *Water_iccv* from [2].

Additionally, we will discuss the performance of the proposed restoration method when the medium is changed to water. As suggested in [1], compared with atmospheric turbulence, the geometric warping effect produced by water is much stronger while the blur effect is relatively milder. Therefore, we apply the proposed method to recover the original image of an underwater scene to test whether it can handle the large geometric deformation. The Twostage method is originally designed for seeing through water, so we compare the performance between the Twostage and our method in one standard underwater sequence ($256 \times 256 \times 61$) from [2]. Fig. 3 shows the results of the two methods, where the Figs. (d) and (e) compare the quality of the reference images, and the Figs. (f) and (g) compare the visual quality of the final outputs. The circular regions in Figs. (d) and (e) demonstrate the low-rank decomposed reference image is a bit sharper than the average image. As is shown in Fig. 3 (g), it is clear that all the characters contained in the scene can be easily recognized except for few characters of the word “Reconstruction” on the lower boundary of the image. This simple test demonstrates the proposed method also can be used to tackle the *seeing through water* problem. However, it is still necessary to adapt the proposed method to the water case, this is our future direction.

II. APPENDIX

A. Total Variation and Nonlocal Total Variation Regularizer

a) *Total Variation Regularizer*: In the proposed restoration model, we impose a total variation regularizer on the difference between the current restored image u and the restored u_p in the previous iterative step. In other

words, such regularizer will promote the sparsity in temporal domain in order to provide a smooth motion pattern between the consecutive restoration steps.

$$J_t(u) = |(u - u_p)|_{TV} = \|\nabla_x(u - u_p)\|_1 + \|\nabla_y(u - u_p)\|_1 \quad (1)$$

where the subscript x and y represent the vertical and the horizontal component of the image domain. The difference operator ∇_x is given by $\nabla_x u(1, j) = 0$ for $j = 1, \dots, N$ and

$$\nabla_x u(i, j) = u(i, j) - u(i - 1, j), \quad i = 2, \dots, N, \quad j = 1, \dots, N.$$

Similarly, ∇_y is the difference operator given by $\nabla_y u(i, 1) = 0$ for $i = 1, \dots, N$ and

$$\nabla_y u(i, j) = u(i, j) - u(i, j - 1), \quad i = 1, \dots, N, \quad j = 2, \dots, N.$$

Here, we define the conjugate operators of ∇_x and ∇_y respectively, they are ∇_x^T and ∇_y^T .

$$\nabla_x^T = \begin{cases} -u(2, j) & \text{if } i = 1 \\ u(i, j) - u(i + 1, j) & \text{if } i = 2, \dots, N - 1 \\ u(N, j) & \text{if } i = N \end{cases} \quad (2)$$

Similarly, the linear operator ∇_y^T is given by

$$\nabla_y^T = \begin{cases} -u(i, 2) & \text{if } j = 1 \\ u(i, j) - u(i, j + 1) & \text{if } j = 2, \dots, N - 1 \\ u(i, N) & \text{if } j = N \end{cases} \quad (3)$$

Let's define the discrete Laplace operator $\Delta := -\nabla_x^T \nabla_x - \nabla_y^T \nabla_y$. For $1 < i, j < N$,

$$-\Delta u(i, j) = \begin{cases} 2u(1, 1) - u(1, 2) - u(2, 1) & \text{if } i = 1, j = 1 \\ 3u(1, j) - u(2, j) - u(1, j - 1) - u(1, j + 1) & \text{if } i = 1, 1 < j < N \\ 3u(i, 1) - u(i, 2) - u(i - 1, 1) - u(i + 1, 1) & \text{if } 1 < i < N, j = 1 \\ 4u(i, j) - u(i + 1, j) - u(i - 1, j) - u(i, j + 1) - u(i, j - 1) & \text{if } 1 < i < N, 1 < j < N \end{cases} \quad (4)$$

b) Nonlocal Total Variation Regularizer: Suppose the digital image model by a graph (Ω, E) , where Ω is a finite set of N nodes (pixels), E is the set of edges. The notation $x \sim y$ is used to denote the edge between the nodes x and y . An image u is a function defined on Ω , which can be represented by a column vector, then the value at node x can be denoted by $u(x)$. In the following, we consider a weight function $w(x, y)$ for the edge $x \sim y \in E$. The weight function is symmetric and can be set to 0 if two nodes x and y are not connected. In this case, unlike classical total variation, nodes of NLTV may directly interact with nodes that are not neighbors. That is why it called “nonlocal”.

For a given image $u(x)$ defined on Ω , the weight graph gradient $\nabla_w u(x)$ is defined as the vector of all directional derivatives (or edge derivative) $\nabla_w u(x, \cdot)$ at x :

$$\nabla_w u(x) := (\nabla_w u(x, y))_{y \in \Omega}$$

where

$$\nabla_w u(x, y) := (u(y) - u(x))\sqrt{w(x, y)}, \forall y \in \Omega$$

The directional derivatives apply to all the nodes y since the weight $w(x, y)$ is extended to the whole domain $\Omega \times \Omega$.

A graph divergence div_w of a vector $p : \Omega \times \Omega \rightarrow R$ can be defined as follows:

$$div_w p(x) = \sum_{y \in \Omega} (p(x, y) - p(y, x))\sqrt{w(x, y)}$$

Then, the graph Laplacian is defined by:

$$\Delta_w u(x) := \frac{1}{2} div_w (\nabla_w u(x)) = \sum_{y \in \Omega} (u(y) - u(x))w(x, y)$$

Using the notations above, the nonlocal total variation can be defined as follows:

$$J_s(u) = J_{NLTV}(u) := \sum_{x \in \Omega} |\nabla_w u(x)| = \sum_{x \in \Omega} \sqrt{\sum_{y \in \Omega} (u(x) - u(y))^2 w(x, y)} \quad (5)$$

B. Solve the Mixed-ROF Model Using Split Bregman

The optimization problem can be expanded as follows:

$$\min_u \mu_1 |\nabla_w u|_1 + \mu_2 (|\nabla_x(u - u_p)|_1 + |\nabla_y(u - u_p)|_1) + \frac{1}{2} \|u - v\|_2^2 \quad (6)$$

To apply Bregman Splitting, we first replace $\nabla_w u$ by d_w , $\nabla_x(u - u_p)$ by d_x and $\nabla_y(u - u_p)$ by d_y . This yields a constrained problem:

$$\min_u \mu_1 |d_w| + \mu_2 |d_x| + \mu_2 |d_y| + \frac{1}{2} \|u - v\|_2^2, \text{ such that } d_w = \nabla_w u, d_x = \nabla_x(u - u_p) \text{ and } d_y = \nabla_y(u - u_p)$$

Then, convert the above problem to the unconstrained problem:

$$\min_{u, d_w, d_x, d_y} \mu_1 |d_w| + \mu_2 |d_x| + \mu_2 |d_y| + \frac{1}{2} \|u - v\|_2^2 + \frac{\lambda_1}{2} \|d_w - \nabla_w u\|_2^2 + \frac{\lambda_2}{2} \|d_x - \nabla_x(u - u_p)\|_2^2 + \frac{\lambda_2}{2} \|d_y - \nabla_y(u - u_p)\|_2^2$$

By applying the Bregman iteration:

$$\min_{u, d_w, d_x, d_y} \mu_1 |d_w| + \mu_2 |d_x| + \mu_2 |d_y| + \frac{1}{2} \|u - v\|_2^2 + \frac{\lambda_1}{2} \|d_w - \nabla_w u - b_w^k\|_2^2 + \frac{\lambda_2}{2} \|d_x - \nabla_x(u - u_p) - b_x^k\|_2^2 + \frac{\lambda_2}{2} \|d_y - \nabla_y(u - u_p) - b_y^k\|_2^2 \quad (7)$$

Then the above problem is equivalent to

$$\begin{aligned} (u^{k+1}, d_w^{k+1}, d_x^{k+1}, d_y^{k+1}) &= \operatorname{argmin}_{u, d_w, d_x, d_y} \mu_1 |d_w| + \mu_2 |d_x| + \mu_2 |d_y| + \frac{1}{2} \|u - v\|_2^2 + \frac{\lambda_1}{2} \|d_w - \nabla_w u - b_w^k\|_2^2 \\ &\quad + \frac{\lambda_2}{2} \|d_x - \nabla_x(u - u_p) - b_x^k\|_2^2 + \frac{\lambda_2}{2} \|d_y - \nabla_y(u - u_p) - b_y^k\|_2^2 \\ b_w^{k+1} &= b_w^k + \nabla_w u^{k+1} - d_w^{k+1} \\ b_x^{k+1} &= b_x^k + \nabla_x u^{k+1} - \nabla_x u_p - d_x^{k+1} \\ b_y^{k+1} &= b_y^k + \nabla_y u^{k+1} - \nabla_y u_p - d_y^{k+1} \end{aligned} \quad (8)$$

The solution of (8) is obtained by performing an alternative minimizing process:

$$u^{k+1} = \underset{u}{\operatorname{argmin}} \frac{1}{2} \|u - v\|_2^2 + \frac{\lambda_1}{2} \|d_w - \nabla_w u - b_w^k\|_2^2 \quad (9)$$

$$+ \frac{\lambda_2}{2} \|d_x - \nabla_x(u - u_p) - b_x^k\|_2^2 + \frac{\lambda}{2} \|d_y - \nabla_y(u - u_p) - b_y^k\|_2^2$$

$$d_w^{k+1} = \underset{d_w}{\operatorname{argmin}} \mu_1 |d_w| + \frac{\lambda_1}{2} \|d_w - \nabla_w u^{k+1} - b_w^k\|_2^2 \quad (10)$$

$$d_x^{k+1} = \underset{d_x}{\operatorname{argmin}} \mu_2 |d_x| + \frac{\lambda_2}{2} \|d_x - \nabla_x(u^{k+1} - u_p) - b_x^k\|_2^2 \quad (11)$$

$$d_y^{k+1} = \underset{d_y}{\operatorname{argmin}} \mu_2 |d_y| + \frac{\lambda_2}{2} \|d_y - \nabla_y(u^{k+1} - u_p) - b_y^k\|_2^2 \quad (12)$$

Now, the subproblem (9) for u^{k+1} consists in solving the linear system:

$$(I - 2\lambda_1 \Delta_w - \lambda_2 \Delta) u^{k+1} = v + \lambda_1 \operatorname{div}_w(b_w^k - d_w^k) + \lambda_2 \nabla_x^T(d_x^k + \nabla_x u_p - b_x^k) \quad (13)$$

$$+ \lambda_2 \nabla_y^T(d_y^k + \nabla_y u_p - b_y^k)$$

$$u^{k+1} = (I - 2\lambda_1 \Delta_w - \lambda_2 \Delta)^{-1} (v + \lambda_1 \operatorname{div}_w(b_w^k - d_w^k) + \lambda_2 \nabla_x^T(d_x^k + \nabla_x u_p - b_x^k) \quad (14)$$

$$+ \lambda_2 \nabla_y^T(d_y^k + \nabla_y u_p - b_y^k))$$

$$d_w^{k+1} = \operatorname{shrink}\left(\nabla_w u^{k+1} + b_w^k, \frac{\mu_1}{\lambda_1}\right) \quad (15)$$

$$d_x^{k+1} = \operatorname{shrink}\left(\nabla_x u^{k+1} - \nabla_x u_p + b_x^k, \frac{\mu_2}{\lambda_2}\right) \quad (16)$$

$$d_y^{k+1} = \operatorname{shrink}\left(\nabla_y u^{k+1} - \nabla_y u_p + b_y^k, \frac{\mu_2}{\lambda_2}\right) \quad (17)$$

C. Solve the Mixed-ROF Model without PDE

We will propose a new iteration schema without involving PDE computing in order to find the unique solution u^* for the minimization problem:

$$\min_u \mu_1 |\nabla_w u|_1 + \mu_2 |\nabla_x(u - u_p)|_1 + \mu_2 |\nabla_y(u - u_p)|_1 + \frac{1}{2} \|u - v\|_2^2 \quad (18)$$

Let $b_w^0 = 0, b_x^0 = 0, b_y^0 = 0$ and $u^1 = v$, for $k = 1, 2, \dots$, the iteration is following:

$$b_w^k = \operatorname{cut}\left(\nabla_w u^k + b_w^{k-1}, \frac{\mu_1}{\lambda_1}\right) \quad (19)$$

$$b_x^k = \operatorname{cut}\left(\nabla_x u^k - \nabla_x u_p + b_x^{k-1}, \frac{\mu_2}{\lambda_2}\right) \quad (20)$$

$$b_y^k = \operatorname{cut}\left(\nabla_y u^k - \nabla_y u_p + b_y^{k-1}, \frac{\mu_2}{\lambda_2}\right) \quad (21)$$

$$u^{k+1} = v + \frac{\lambda_1}{\mu_1} \operatorname{div}_w b_w^k - \frac{\lambda_2}{\mu_2} (\nabla_x^T b_x^k + \nabla_y^T b_y^k) \quad (22)$$

where the function $cut(\cdot)$ defined as follows:

$$cut(c, 1/\lambda) = \begin{cases} 1/\lambda & \text{for } c > 1/\lambda \\ c & \text{for } -1/\lambda \leq c \leq 1/\lambda \\ -1/\lambda & \text{for } c < -1/\lambda \end{cases} \quad (23)$$

Lemma 1. *Given $0 < 20\lambda_1 + 4\lambda_2 < 1$, the real symmetric linear operator $I + 2\lambda_1\Delta_w + \lambda_2\Delta$ is positive definite.*

Proof: Suppose that η is an eigenvalue of the operator $I + 2\lambda_1\Delta_w + \lambda_2\Delta$. Then, we want to validate $\eta > 0$ when $0 < 20\lambda_1 + 4\lambda_2 < 1$. There exists a nonzero vector $u \in \mathbb{R}^{N^2}$ such that $(I + 2\lambda_1\Delta_w + \lambda_2\Delta)u = \eta u$. It follows that $(I - \eta)u = -2\lambda_1\Delta_w u - \lambda_2\Delta u$. Let $m = \|u\|_\infty = \max_{1 \leq i, j \leq N} |u(i, j)|$. There exist $i_0, j_0 \in \{1, \dots, N\}$ such that $|u(i_0, j_0)| = m$. If $\eta \leq 0$, then $|(1 - \eta)u(i_0, j_0)| \geq m$. On the other hand, $|-2\lambda_1\Delta_w u(i_0, j_0) - \lambda_2\Delta u(i_0, j_0)| \leq (20\lambda_1 + 4\lambda_2)m$ (In practice, we choose 10 neighbors for NLTV and 4 neighbors for TV in image domain). Hence, $m \leq (20\lambda_1 + 4\lambda_2)m$. Since $0 < 20\lambda_1 + 4\lambda_2 < 1$, it is obvious that $m = 0$ which means $u = 0$. Therefore, any eigenvalue of $(\mu + 2\lambda\Delta_w + \lambda\Delta)$ is positive. The $I + 2\lambda_1\Delta_w + \lambda_2\Delta$ is positive definite. \blacksquare

We would demonstrate that the algorithm given by (19), (20), (21) and (22) has the equivalent formulation described as follows:

Let $d_w^k = d_x^k = d_y^k = 0$, $b_w^k = b_x^k = b_y^k = 0$, $u^1 = v$. For $k = 1, 2, \dots$, let

$$d_w^k = \operatorname{argmin}_{d_w} \left\{ \mu_1 \|d_w\|_1 + \frac{\lambda_1}{2} \|d_w - \nabla_w u^k - b_w^{k-1}\| \right\} \quad (24)$$

$$d_x^k = \operatorname{argmin}_{d_x} \left\{ \mu_2 \|d_x\|_1 + \frac{\lambda_2}{2} \|d_x - \nabla_x (u^k - u_p) - b_x^{k-1}\| \right\} \quad (25)$$

$$d_y^k = \operatorname{argmin}_{d_y} \left\{ \mu_2 \|d_y\|_1 + \frac{\lambda_2}{2} \|d_y - \nabla_y (u^k - u_p) - b_y^{k-1}\| \right\} \quad (26)$$

$$b_w^k = \nabla_w u^k + b_w^{k-1} - d_w^k \quad (27)$$

$$b_x^k = \nabla_x u^k - \nabla_x u_p + b_x^{k-1} - d_x^k \quad (28)$$

$$b_y^k = \nabla_y u^k - \nabla_y u_p + b_y^{k-1} - d_y^k \quad (29)$$

$$\begin{aligned} u^{k+1} = \operatorname{argmin}_u & \left\{ \frac{1}{2} \|B(u - v)\|_2^2 - \langle B^2(u^k - v), u - u^k \rangle + \frac{\lambda_1}{2\mu_1} \|d_w^k - \nabla_w u\|_2^2 \right. \\ & \left. + \frac{\lambda_2}{2\mu_2} \|d_x^k - \nabla_x u + \nabla_x u_p\|_2^2 + \frac{\lambda_2}{2\mu_2} \|d_y^k - \nabla_y u + \nabla_y u_p\| \right\} \end{aligned} \quad (30)$$

where $B = I + 2\lambda_1\Delta_w + \lambda_2\Delta$. Actually, the value of u_p depends on the iteration k rather than the the value of u .

Lemma 2. *For $k = 1, 2, \dots$, let $d_w^k, d_x^k, d_y^k, b_w^k, b_x^k, b_y^k$ and u^{k+1} be given by the iteration (19) to (22). Then $\lim_{k \rightarrow \infty} (u^{k+1} - u^k) = 0$, and*

$$b_w^k = cut(\nabla_w u^k + b_w^{k-1}, \frac{\mu_1}{\lambda_1})$$

$$b_x^k = cut(\nabla_x u^k - \nabla_x u_p + b_x^{k-1}, \frac{\mu_2}{\lambda_2})$$

$$b_y^k = cut(\nabla_y u^k - \nabla_y u_p + b_y^{k-1}, \frac{\mu_2}{\lambda_2})$$

Proof: According to (24) ~ (26), we can obtain the following:

$$d_w^k = \mathit{shrink}\left(\nabla_w u^k + b_w^{k-1}, \frac{\mu_1}{\lambda_1}\right) \quad (31)$$

$$d_x^k = \mathit{shrink}\left(\nabla_x u^k - \nabla_x u_p + b_x^{k-1}, \frac{\mu_2}{\lambda_2}\right) \quad (32)$$

$$d_y^k = \mathit{shrink}\left(\nabla_y u^k - \nabla_y u_p + b_y^{k-1}, \frac{\mu_2}{\lambda_2}\right) \quad (33)$$

Combining the (31) with (27):

$$\begin{aligned} b_w^k &= \nabla_w u^k + b_w^{k-1} - d_w^k \\ &= \nabla_w u^k + b_w^{k-1} - \mathit{shrink}\left(\nabla_w u^k + b_w^{k-1}, \frac{\mu_1}{\lambda_1}\right) \\ &= \mathit{cut}\left(\nabla_w u^k + b_w^{k-1}, \frac{\mu_1}{\lambda_1}\right) \end{aligned}$$

Similarly, we can get the Eqn.20 and 21. Therefore, $\|b_w^k\|_\infty \leq \mu_1/\lambda_1$, $\|b_x^k\|_\infty \leq \mu_2/\lambda_2$ and $\|b_y^k\|_\infty \leq \mu_2/\lambda_2$ for $k = 1, 2, \dots$

Suppose $G(d) := \|d\|_1$ for $d \in \mathbb{R}^{N^2}$. let $g_w^k = \frac{\lambda_1}{\mu_1} b_w^k$, $g_x^k = \frac{\lambda_2}{\mu_2} b_x^k$ and $g_y^k = \frac{\lambda_2}{\mu_2} b_y^k$. From the (24) and (27), we can get

$$g_w^k = g_w^{k-1} - \frac{\lambda_1}{\mu_1} (d_w^k - \nabla_w u^k) = -\frac{\lambda_1}{\mu_1} (d_w^k - \nabla_w u^k - b_w^{k-1}) \in \partial G(d_w^k)$$

So, $g_w^k - \frac{\lambda_1}{\mu_1} (d_w^{k+1} - \nabla_w u^{k+1}) \in \partial G(d_w^{k+1})$ and

$$d_w^{k+1} = \operatorname{argmin}_{d_w} \{ \|d_w\|_1 - \langle g_w^k, d_w - d_w^k \rangle + \frac{\lambda_1}{2\mu_1} \|d_w - \nabla_w u^{k+1}\|_2^2 \} \quad (34)$$

The same to

$$d_x^{k+1} = \operatorname{argmin}_{d_x} \{ \|d_x\|_1 - \langle g_x^k, d_x - d_x^k \rangle + \frac{\lambda_2}{2\mu_2} \|d_x - \nabla_x u^{k+1} + \nabla_x u_p\|_2^2 \} \quad (35)$$

$$d_y^{k+1} = \operatorname{argmin}_{d_y} \{ \|d_y\|_1 - \langle g_y^k, d_y - d_y^k \rangle + \frac{\lambda_2}{2\mu_2} \|d_y - \nabla_y u^{k+1} + \nabla_y u_p\|_2^2 \} \quad (36)$$

It follows from (34), (35) and (36) that

$$\begin{aligned} \|d_w^{k+1}\|_1 - \langle g_w^k, d_w^{k+1} - d_w^k \rangle + \frac{\lambda_1}{2\mu_1} \|d_w^{k+1} - \nabla_w u^{k+1}\|_2^2 &\leq \|d_w^k\|_1 + \frac{\lambda_1}{2\mu_1} \|d_w^k - \nabla_w u^{k+1}\|_2^2 \\ \|d_x^{k+1}\|_1 - \langle g_x^k, d_x^{k+1} - d_x^k \rangle + \frac{\lambda_2}{2\mu_2} \|d_x^{k+1} - \nabla_x u^{k+1} + \nabla_x u_p\|_2^2 &\leq \|d_x^k\|_1 + \frac{\lambda_2}{2\mu_2} \|d_x^k - \nabla_x u^{k+1} + \nabla_x u_p\|_2^2 \\ \|d_y^{k+1}\|_1 - \langle g_y^k, d_y^{k+1} - d_y^k \rangle + \frac{\lambda_2}{2\mu_2} \|d_y^{k+1} - \nabla_y u^{k+1} + \nabla_y u_p\|_2^2 &\leq \|d_y^k\|_1 + \frac{\lambda_2}{2\mu_2} \|d_y^k - \nabla_y u^{k+1} + \nabla_y u_p\|_2^2 \end{aligned}$$

Since $g_w^k \in \partial G(d_w^k)$, $g_x^k \in \partial G(d_x^k)$ and $g_y^k \in \partial G(d_y^k)$, by the definition of the Bregman Distance we can get

$$\frac{\lambda_1}{2\mu_1} \|d_w^{k+1} - \nabla_w u^{k+1}\|_2^2 \leq \frac{\lambda_1}{2\mu_1} \|d_w^k - \nabla_w u^{k+1}\|_2^2 \quad (37)$$

$$\frac{\lambda_2}{2\mu_2} \|d_x^{k+1} - \nabla_x u^{k+1} + \nabla_x u_p\|_2^2 \leq \frac{\lambda_2}{2\mu_2} \|d_x^k - \nabla_x u^{k+1} + \nabla_x u_p\|_2^2 \quad (38)$$

$$\frac{\lambda_2}{2\mu_2} \|d_y^{k+1} - \nabla_y u^{k+1} + \nabla_y u_p\|_2^2 \leq \frac{\lambda_2}{2\mu_2} \|d_y^k - \nabla_y u^{k+1} + \nabla_y u_p\|_2^2 \quad (39)$$

By (30) we achieve the following inequality

$$\begin{aligned} & \frac{1}{2} \|B(u^{k+1} - v)\|_2^2 - \langle B^2(u^k - v), u^{k+1} - u^k \rangle + \frac{\lambda_1}{2\mu_1} \|d_w^k - \nabla_w u^{k+1}\|_2^2 + \frac{\lambda_2}{2\mu_2} \|d_x^k - \nabla_x u^{k+1} + \nabla_x u_p\|_2^2 \\ & + \frac{\lambda_2}{2\mu_2} \|d_y^k - \nabla_y u^{k+1} + \nabla_y u_p\|_2^2 \leq \frac{1}{2} \|B(u - v)\|_2^2 - \langle B^2(u^k - v), u - u^k \rangle + \frac{\lambda_1}{2\mu_1} \|d_w^k - \nabla_w u\|_2^2 \\ & + \frac{\lambda_2}{2\mu_2} \|d_x^k - \nabla_x u + \nabla_x u_p\|_2^2 + \frac{\lambda_2}{2\mu_2} \|d_y^k - \nabla_y u + \nabla_y u_p\|_2^2 \end{aligned}$$

Choosing $u = u^k$ and replacing the u_p according to u in the above inequality, we obtain

$$\begin{aligned} & \frac{1}{2} \|B(u^{k+1} - v)\|_2^2 - \langle B(u^k - v), B(u^{k+1} - u^k) \rangle + \frac{\lambda_1}{2\mu_1} \|d_w^k - \nabla_w u^{k+1}\|_2^2 + \frac{\lambda_2}{2\mu_2} \|d_x^k - \nabla_x u^{k+1} + \nabla_x u^k\|_2^2 \\ & + \frac{\lambda_2}{2\mu_2} \|d_y^k - \nabla_y u^{k+1} + \nabla_y u^k\|_2^2 \leq \frac{1}{2} \|B(u^k - v)\|_2^2 + \frac{\lambda_1}{2\mu_1} \|d_w^k - \nabla_w u^k\|_2^2 \\ & + \frac{\lambda_2}{2\mu_2} \|d_x^k - \nabla_x u^k + \nabla_x u^{k-1}\|_2^2 + \frac{\lambda_2}{2\mu_2} \|d_y^k - \nabla_y u^k + \nabla_y u^{k-1}\|_2^2 \end{aligned}$$

Since

$$\frac{1}{2} \|B(u^{k+1} - v)\|_2^2 - \frac{1}{2} \|B(u^k - v)\|_2^2 - \langle B(u^k - v), B(u^{k+1} - u^k) \rangle = \frac{1}{2} \|B(u^{k+1} - u^k)\|_2^2$$

Thus, we deduce that

$$\begin{aligned} & \frac{1}{2} \|B(u^{k+1} - u^k)\|_2^2 + \frac{\lambda_1}{2\mu_1} \|d_w^k - \nabla_w u^{k+1}\|_2^2 + \frac{\lambda_2}{2\mu_2} \|d_x^k - \nabla_x u^{k+1} + \nabla_x u^k\|_2^2 \\ & + \frac{\lambda_2}{2\mu_2} \|d_y^k - \nabla_y u^{k+1} + \nabla_y u^k\|_2^2 \leq \gamma_k, k = 1, 2, \dots \end{aligned}$$

where

$$\gamma_k = \frac{\lambda_1}{2\mu_1} \|d_w^k - \nabla_w u^k\|_2^2 + \frac{\lambda_2}{2\mu_2} \|d_x^k - \nabla_x u^k + \nabla_x u^{k-1}\|_2^2 + \frac{\lambda_2}{2\mu_2} \|d_y^k - \nabla_y u^k + \nabla_y u^{k-1}\|_2^2 \quad (40)$$

This together with (37) ~ (39) gives:

$$\frac{1}{2} \|B(u^{k+1} - u^k)\|_2^2 + \gamma_{k+1} \leq \gamma_k \quad (41)$$

This indicates that $\gamma_1 \geq \gamma_2 \geq \dots$ and $\gamma_k \geq 0$ for all k . Therefore, $\lim_{k \rightarrow \infty} \gamma_k$ exists. Since B is positive definite, we can achieve that $\lim_{k \rightarrow \infty} (u^{k+1} - u^k) = 0$. \blacksquare

Lemma 3. For $k = 1, 2, \dots$, let $d_w^k, d_x^k, d_y^k, b_w^k, b_x^k, b_y^k$ and u^{k+1} be given by the iteration (19) to (22). Then all the sequences $(d_w^k)_{k=1,2,\dots}, (d_x^k)_{k=1,2,\dots}, (d_y^k)_{k=1,2,\dots}, (b_w^k)_{k=1,2,\dots}, (b_x^k)_{k=1,2,\dots}, (b_y^k)_{k=1,2,\dots}$ and $(u^k)_{k=1,2,\dots}$ are bounded. Moreover,

$$u^{k+1} = v + \frac{\lambda_1}{\mu_1} \text{div}_w b_w^k - \frac{\lambda_2}{\mu_2} (\nabla_x^T b_x^k + \nabla_y^T b_y^k)$$

Proof: It is proved that $\|b_w^k\|_\infty \leq \mu_1/\lambda_1, \|b_x^k\|_\infty \leq \mu_2/\lambda_2$ and $\|b_y^k\|_\infty \leq \mu_2/\lambda_2$. Differentiate the right part of the (30) and set to zero, we have

$$\begin{aligned} & B^2(u - v) - B^2(u^k - v) + \frac{\lambda_1}{\mu_1} \text{div}_w (d_w^k - \nabla_w u) \\ & - \frac{\lambda_2}{\mu_2} \nabla_x^T (d_x^k - \nabla_x u + \nabla_x u_p) - \frac{\lambda_2}{\mu_2} \nabla_y^T (d_y^k - \nabla_y u + \nabla_y u_p) = 0 \end{aligned}$$

Choosing $u = u^{k+1}$, the above equation can be reformulated as

$$B^2(u^{k+1} - u^k) - 2\frac{\lambda_1}{\mu_1}\Delta_w u^{k+1} - \frac{\lambda_2}{\mu_2}\Delta u^{k+1} = \frac{\lambda_2}{\mu_2}(\nabla_x^T d_x^k + \nabla_x^T d_y^k) - \frac{\lambda_1}{\mu_1}\text{div}_w d_w^k - \frac{\lambda_2}{\mu_2}\Delta u_p$$

Since $B^2 = (I + 2\lambda\Delta_w + \lambda\Delta)$, we have

$$(u^{k+1} - u^k) = \frac{\lambda_2}{\mu_2}(\nabla_x^T d_x^k + \nabla_x^T d_y^k) + \frac{\lambda_2}{\mu_2}\Delta u^k - \frac{\lambda_2}{\mu_2}\Delta u_p - \frac{\lambda_1}{\mu_1}\text{div}_w d_w^k + 2\frac{\lambda_1}{\mu_1}\Delta_w u^k$$

Using (27) to (29), we can reformulate the above equation as follows

$$(u^{k+1} - u^k) = \frac{\lambda_2}{\mu_2}\nabla_x^T(b_x^{k-1} - b_x^k) + \frac{\lambda_2}{\mu_2}\nabla_y^T(b_y^{k-1} - b_y^k) - \frac{\lambda_1}{\mu_1}\text{div}_w(b_w^{k-1} - b_w^k)$$

It follows that

$$\sum_{k=1}^n (u^{k+1} - u^k) = \sum_{k=1}^n \left[\frac{\lambda_2}{\mu_2}\nabla_x^T(b_x^{k-1} - b_x^k) + \frac{\lambda_2}{\mu_2}\nabla_y^T(b_y^{k-1} - b_y^k) - \frac{\lambda_1}{\mu_1}\text{div}_w(b_w^{k-1} - b_w^k) \right]$$

Since $u^1 = v$, the above equation reduce to

$$u^{n+1} - v = -\frac{\lambda_2}{\mu_2}\nabla_x^T b_x^n - \frac{\lambda_2}{\mu_2}\nabla_y^T b_y^n + \frac{\lambda_1}{\mu_1}\text{div}_w b_w^n$$

Hence, we can get the (22). Since $\|b_w^k\|_\infty$, $\|b_x^k\|_\infty$ and $\|b_y^k\|_\infty$ are bounded, we have the sequence $(u^k)_{k=1,2,\dots}$ is bounded. Moreover, by (27) to (29) the sequence $(d_w^k)_{k=1,2,\dots}$, $(d_x^k)_{k=1,2,\dots}$ and $(d_y^k)_{k=1,2,\dots}$ are also bounded. ■

Lemma 4. For $k = 1, 2, \dots$, let $d_w^k, d_x^k, d_y^k, b_w^k, b_x^k, b_y^k$ and u^{k+1} be given by the iteration (19) to (22). Then

$$\begin{aligned} \lim_{k \rightarrow \infty} (d_w^k - \nabla_w u^k) &= 0 \\ \lim_{k \rightarrow \infty} (d_x^k - \nabla_x (u^k - u_p)) &= 0 \\ \lim_{k \rightarrow \infty} (d_y^k - \nabla_y (u^k - u_p)) &= 0 \end{aligned}$$

Proof: For $G(d_x) = \|d\|_1$, since $g_x^k = \frac{\lambda_2}{\mu_2}b_x^k \in \partial G(d_x^k)$, $k = 1, 2, \dots$, we can get

$$\begin{aligned} &[G(d_x) - G(d_x^{k+1}) - \langle g_x^{k+1}, d_x - d_x^{k+1} \rangle] - [G(d_x) - G(d_x^k) - \langle g_x^k, d_x - d_x^k \rangle] \\ &+ [G(d_x^{k+1}) - G(d_x^k) - \langle g_x^k, d_x^{k+1} - d_x^k \rangle] = \langle g_x^k - g_x^{k+1}, d - d_x^{k+1} \rangle \end{aligned}$$

Since $G(d_x^{k+1}) - G(d_x^k) - \langle g_x^k, d_x^{k+1} - d_x^k \rangle \geq 0$, we have

$$\langle g_x^k - g_x^{k+1}, d - d_x^{k+1} \rangle \geq -\|d_x^{k+1}\|_1 - \langle g_x^{k+1}, d - d_x^{k+1} \rangle + \|d_x^k\|_1 + \langle g_x^k, d - d_x^k \rangle \quad (42)$$

Choosing $u_p = u^k$, the (28) indicates that $g_x^k - g_x^{k+1} = \frac{\lambda_2}{\mu_2}(d_x^{k+1} - \nabla_x u^{k+1} + \nabla_x u^k)$. Thus, by Bregman Distance we have

$$\frac{\lambda_2}{2\mu_2}\|d_x - \nabla_x u^{k+1} + \nabla_x u^k\|_2^2 + \frac{\lambda_2}{2\mu_2}\|d_x^{k+1} - \nabla_x u^{k+1} + \nabla_x u^k\|_2^2 - \langle g_x^k - g_x^{k+1}, d_x - d_x^{k+1} \rangle \geq 0 \quad (43)$$

From (42) and (43), we have

$$\begin{aligned} &\frac{\lambda_2}{2\mu_2}\|d_x - \nabla_x u^{k+1} + \nabla_x u^k\|_2^2 + \frac{\lambda_2}{2\mu_2}\|d_x^{k+1} - \nabla_x u^{k+1} + \nabla_x u^k\|_2^2 \geq \\ &\quad -\|d_x^{k+1}\|_1 - \langle g_x^{k+1}, d_x - d_x^{k+1} \rangle + \|d_x^k\|_1 + \langle g_x^k, d_x - d_x^k \rangle \end{aligned}$$

Choosing $d_x = \nabla_x u^{k+1} - \nabla_x u^k$ and defining $\beta_k = \langle g_x^k, \nabla_x u^k - \nabla_x u^{k-1} - d_x^k \rangle$, we have

$$\begin{aligned} \frac{\lambda_2}{2\mu_2} \|d_x^{k+1} - \nabla_x(u^{k+1} - u^k)\|_2^2 &\leq (\|d_x^{k+1}\|_1 - \|d_x^k\|_1) + (\beta_{k+1} - \beta_k) \\ &\quad - \langle g_x^k, (\nabla_x u^{k+1} - \nabla_x u^k) - (\nabla_x u^k - \nabla_x u^{k-1}) \rangle \end{aligned}$$

Therefore, for $1 \leq m \leq n$, we can get

$$\begin{aligned} \sum_{k=m}^{n-1} \frac{\lambda_2}{2\mu_2} \|d_x^{k+1} - \nabla_x(u^{k+1} - u^k)\|_2^2 &\leq \sum_{k=m}^{n-1} [(\|d_x^{k+1}\|_1 - \|d_x^k\|_1) + (\beta_{k+1} - \beta_k) \\ &\quad - \langle g_x^k, (\nabla_x u^{k+1} - \nabla_x u^k) - (\nabla_x u^k - \nabla_x u^{k-1}) \rangle] \end{aligned}$$

Then

$$\begin{aligned} \sum_{k=m}^{n-1} \frac{\lambda_2}{2\mu_2} \|d_x^{k+1} - \nabla_x(u^{k+1} - u^k)\|_2^2 &\leq (\|d_x^n\|_1 - \|d_x^m\|_1) + (\beta_n - \beta_m) \\ &\quad - \sum_{k=m}^{n-1} [\langle g_x^k, (\nabla_x u^{k+1} - \nabla_x u^k) - (\nabla_x u^k - \nabla_x u^{k-1}) \rangle] \end{aligned}$$

Recall Lemma 3, the sequences $(d_x^k)_{k=1,2,\dots}, (g_x^k)_{k=1,2,\dots}, (u^k)_{k=1,2,\dots}$ are bounded, there exist positive constants C_1 and C_2 independent of n and m such that

$$\sum_{k=m}^{n-1} \frac{\lambda_2}{2\mu_2} \|d_x^{k+1} - \nabla_x(u^{k+1} - u^k)\|_2^2 \leq C_1 + C_2(n-m)\eta_m \quad (44)$$

where $\eta_m := \sup_{m \leq k} \|u^{k+1} - u^k\|_2$. Combining the Lemma 2, we have $\lim_{m \rightarrow \infty} \eta_m = 0$. The same way to d_w and d_y :

$$\sum_{k=m}^{n-1} \frac{\lambda_1}{2\mu_1} \|d_w^{k+1} - \nabla_w u^{k+1}\|_2^2 \leq C_1 + C_2(n-m)\eta_m \quad (45)$$

$$\sum_{k=m}^{n-1} \frac{\lambda_2}{2\mu_2} \|d_y^{k+1} - \nabla_y(u^{k+1} - u^k)\|_2^2 \leq C_1 + C_2(n-m)\eta_m \quad (46)$$

Adding (44), (45) and (46) gives

$$\sum_{k=m}^{n-1} \gamma_{k+1} \leq 3C_1 + 3C_2(n-m)\eta_m$$

Since $\gamma_n \leq \gamma_k$ for $k \leq n$, $(n-m)\gamma_n \leq 3C_1 + 3C_2(n-m)$, that means

$$\gamma_n \leq \frac{3C_1}{n-m} + 3C_2\eta_m$$

The above inequality indicates that $\lim_{n \rightarrow \infty} \gamma_n = 0$ ■

Theorem 1. For $k = 1, 2, \dots$, let b_w^k, b_x^k, b_y^k and u^{k+1} be given by the iteration (19) to (22). If $0 < 20\lambda_1 + 4\lambda_2 < 1$, then $\lim_{k \rightarrow \infty} u^k = u^*$.

Proof: Let $F(u) := (1/2)\|u - v\|_2^2$, then $\partial F(u) = u - v$. For $w \in \mathbb{R}^{N^2}$ we can get

$$F(u^{k+1} + w) - F(u^{k+1}) - \langle u^{k+1} - v, w \rangle \geq 0 \quad (47)$$

From Lemma 3, we have $-(u^{k+1} - v) = \frac{\lambda_2}{\mu_2} \nabla_x^T b_x^k + \frac{\lambda_2}{\mu_2} \nabla_y^T b_y^k - \frac{\lambda_1}{\mu_1} \text{div}_w b_w^k$, and moreover $\langle \text{div}_w p, q \rangle = -\langle p, \nabla_w q \rangle$. Then,

$$F(u^{k+1} + w) - F(u^{k+1}) + \langle \frac{\lambda_2}{\mu_2} b_x^k, \nabla_x w \rangle + \langle \frac{\lambda_2}{\mu_2} b_y^k, \nabla_y w \rangle + \langle \frac{\lambda_1}{\mu_1} b_w^k, \nabla_w w \rangle \geq 0 \quad (48)$$

Recall that $G(d) = \|d\|_1$, $\frac{\lambda_1}{\mu_1} b_w^k \in \partial G(d_w^k)$, $\frac{\lambda_2}{\mu_2} b_x^k \in \partial G(d_x^k)$ and $\frac{\lambda_2}{\mu_2} b_y^k \in \partial G(d_y^k)$, so,

$$\|d_w^k + \nabla_w w\|_1 - \|d_w^k\|_1 - \langle \frac{\lambda_1}{\mu_1} b_w^k, \nabla_w w \rangle \geq 0 \quad (49)$$

$$\|d_x^k + \nabla_x w\|_1 - \|d_x^k\|_1 - \langle \frac{\lambda_2}{\mu_2} b_x^k, \nabla_x w \rangle \geq 0 \quad (50)$$

$$\|d_y^k + \nabla_y w\|_1 - \|d_y^k\|_1 - \langle \frac{\lambda_2}{\mu_2} b_y^k, \nabla_y w \rangle \geq 0 \quad (51)$$

Adding (48) ~ (51) gives

$$\|d_w^k\|_1 + \|d_x^k\|_1 + \|d_y^k\|_1 + F(u^{k+1}) \leq \|d_w^k + \nabla_w w\|_1 + \|d_x^k + \nabla_x w\|_1 + \|d_y^k + \nabla_y w\|_1 + F(u^{k+1} + w) \quad (52)$$

Suppose that $(k_j)_{j=1,2,\dots}$ is an increasing sequence of positive integers such that the sequence $(u^{k_j})_{j=1,2,\dots}$ converges to the limit \tilde{u} . By Lemma 2, we have $\lim_{k \rightarrow \infty} (u^{k+1} - u^k) = 0$. Therefore, $\lim_{j \rightarrow \infty} u^{k_j+1} = \tilde{u}$. Moreover, we have the following via the Lemma 4:

$$\lim_{j \rightarrow \infty} d_w^k = \lim_{j \rightarrow \infty} [(d_w^k - \nabla_w u^k) + \nabla_w u^k] = \nabla_w \tilde{u} \quad (53)$$

also have

$$\lim_{j \rightarrow \infty} d_x^k = \lim_{j \rightarrow \infty} [(d_x^k - \nabla_x (u^k - u_p)) + \nabla_x (u^k - u_p)] = \nabla_x (\tilde{u} - u_p) \quad (54)$$

$$\lim_{j \rightarrow \infty} d_y^k = \lim_{j \rightarrow \infty} [(d_y^k - \nabla_y (u^k - u_p)) + \nabla_y (u^k - u_p)] = \nabla_y (\tilde{u} - u_p) \quad (55)$$

Replacing k by k_j in (52) and let $j \rightarrow \infty$, we have:

$$\begin{aligned} \|\nabla_w \tilde{u}\|_1 + \|\nabla_x (\tilde{u} - u_p)\|_1 + \|\nabla_y (\tilde{u} - u_p)\|_1 + F(\tilde{u}) &\leq \|\nabla_w (\tilde{u} + w)\|_1 + \\ &\|\nabla_x (\tilde{u} - u_p + w)\|_1 + \|\nabla_y (\tilde{u} - u_p + w)\|_1 + F(\tilde{u} + w) \end{aligned}$$

The above equations hold for all the $w \in \mathbb{R}^{N^2}$. On the other hand, u^* is the unique solution to the minimization problem (18). Therefore, we must have $\tilde{u} = u^*$. Since $(u^k)_{k=1,2,\dots}$ is a bounded sequence, we have

$$\lim_{k \rightarrow \infty} u^k = u^*. \quad (56)$$

This completes the proof of the Main Theorem 1. ■

REFERENCES

- [1] X. Zhu, P. Milanfar. Removing atmospheric turbulence via space-invariant deconvolution. *IEEE Trans. on Pattern Analysis and Machine Intelligence*, 157-170(35), 2013.
- [2] Y. Tian, S. G. Narasimhan. Seeing through water: image restoration using model-based tracking. *Computer Vision and Pattern Recognition*, 2303-2310, 2009.